

Notice

This is a non-peer reviewed preprint submitted to EarthArXiv. This manuscript has been submitted to Journal of Geophysical Research - Solid Earth on 2021-03-17 with reference number 2021JB022071. Please check for the most recent version before referencing or citing since subsequent newer versions may differ in text and content

Details

Title: Dilatancy and compaction of a rate-and-state fault in a poroelastic medium: Linearized stability analysis

Authors

- 1 Elias Heimisson (California Institute of Technology/ETH Zurich)
- 2 John Rudnicki (Northwestern University)
- 3 Nadia Lapusta (California Institute of Technology)

Contact: elias.heimisson@sed.ethz.ch

Dilatancy and compaction of a rate-and-state fault in a poroelastic medium: Linearized stability analysis

Elías Rafn Heimisson^{1,2}, John Rudnicki³, Nadia Lapusta^{1,4}

¹Seismological Laboratory, California Institute of Technology, Pasadena, CA, USA

²Now at: Swiss Seismological Service, ETH Zurich, Zurich, Switzerland

³Department of Civil and Environmental Engineering and Department of Mechanical Engineering,

Northwestern University, Evanston, IL, USA

⁴Department of Mechanical and Civil Engineering, California Institute of Technology, Pasadena,

California, USA

Key Points:

- We analyze stability of a rate-and-state fault in a poroelastic solid with fully coupled dilatancy
- We show that dilatancy stabilization can also occur in a highly diffusive bulk if shear zone permeability is low
- We identify a new stabilizing mechanism associated with the mechanical expansion of the shear zone

Corresponding author: Elías Rafn Heimisson, eheimiss@caltech.edu,
elias.heimisson@sed.ethz.ch

Abstract

Faults in the crust at seismogenic depths are embedded in a fluid-saturated, elastic, porous material. Slip on such faults may induce transient pore pressure changes through dilatancy or compaction of the gouge or host rock. However, the poroelastic nature of the crust and the full coupling of inelastic gouge processes and the host rock have been largely neglected in previous analyses. Here, we present a linearized stability analysis of a rate-and-state fault at steady-state sliding in a fully-coupled poroelastic solid under in-plane and anti-plane sliding. We further account for dilatancy of the shear zone and the associated pore pressure changes in an averaged sense. We derive the continuum equivalent of the analysis by Segall and Rice (1995) and highlight a new parameter regime where dilatancy stabilization can act in a highly diffusive solid. Such stabilization is permitted since the time scale of flux through the shear zone and diffusion into the bulk can be very different. A novel aspect of this study involves analyzing the mechanical expansion of the shear layer causing fault-normal displacements, which we describe by a mass balance of the solid constituent of the gouge. This effect gives rise to a universal stabilization mechanism in both drained and undrained limits. The importance of the mechanism scales with shear-zone thickness and it is significant for wider shear zones exceeding approximately 1 cm. We hypothesize that this stabilization mechanism may alter and delay an ongoing shear localization process.

1 Introduction

Recently, the role of fluids in faults has received great interest for two main reasons: first, by the discovery of a strong causal link between fluid injection and induced seismicity (e.g., Ellsworth, 2013); second, by the mounting evidence that slow slip and tremor are generated at high ambient fluid pressures (e.g., Bürgmann, 2018). A topic of notable recent interest in studies of induced seismicity is the role of poroelasticity. The slow slip and tremor literature has been significantly influenced by the idea of dilatancy and how dilatancy can stabilize fault slip and generate slow slip events. Recently, it has become clear that topic of slow slip and aseismic transients in nature and human-induced seismicity are closely linked. For example, Bhattacharya and Viesca (2019) and Viesca and Dublanche (2019) have shown how spontaneous aseismic and slow slip transients arise on faults subject to pore-pressure changes. Torberntsson et al. (2018) investigated slow and fast slip in response to fluid injection near a fault in a poroelastic solid. Fur-

49 ther, dilatancy as a stabilizing mechanism for faults subjected to fluid injection has been
 50 studied recently (Ciardo & Lecampion, 2019). This study combines both poroelasticity
 51 and dilatancy to understand frictional sliding in a fully coupled sense, where pore pres-
 52 sure changes of the shear zone influence the bulk and vice versa. In this introduction,
 53 we start by discussing poroelasticity, then we review the concept of dilatancy, and finally
 54 we provide an overview of the paper.

55 Biot’s theory of poroelasticity has gained much interest in the study of induced seis-
 56 micity (Segall & Lu, 2015) because fluid injection does not only change pore pressure,
 57 but also induces long-ranging stress interactions through the coupling of fluid pressure
 58 and straining of the porous rock. It is well established that the crust behaves as a poroe-
 59 lastic solid (Jónsson et al., 2003) and thus Biot’s theory of poroelasticity offers a more
 60 realistic way to model the earth’s crust than simple elasticity.

61 The role of poroelasticity in the propagation of shear cracks and frictional sliding
 62 has been a subject of interest for decades (Rice & Simons, 1976; Rice & Cleary, 1976;
 63 Rudnicki & Koutsibelas, 1991; Rudnicki & Rice, 2006; Dunham & Rice, 2008; Heimis-
 64 son et al., 2019). Perhaps the most intriguing aspect of this problem is the role of the
 65 pore pressure changes during in-plane, or mode II, sliding. Such sliding induces volumet-
 66 ric stress change on both sides of the fault plane, whereas anti-plane or mode III slid-
 67 ing does not induce volumetric stress. During in-plane sliding, the volumetric stress change
 68 is compressive on one side and expansive on the other, with a discontinuity across the
 69 plane. This raises an important question of which pore pressure should be used to com-
 70 pute the effective normal stress at the frictional interface. Field observations of faults
 71 suggest that the principal slip zone often lies at the boundary of the damage zone and
 72 the fault core (F. M. Chester et al., 1993, 2004; Dor et al., 2006). The fault core gener-
 73 ally has a much lower permeability than the damage zone (Wibberley & Shimamoto, 2003).
 74 In models that idealize the fault core as an impermeable surface, the relevant pore pres-
 75 sure is often taken to be the value at an infinitesimal distance from the shear zone (pre-
 76 sented as p^+ or p^- in Figure 1a but no core depicted) (Rudnicki & Koutsibelas, 1991;
 77 Rudnicki & Rice, 2006; Dunham & Rice, 2008; Heimisson et al., 2019). Another view
 78 was presented by Jha and Juanes (2014), in which shear localization occurs preferentially
 79 in the fault core where effective normal stress is low and thus the relevant pore pressure
 80 is where it is highest on either side of the fault core. However, such a model requires the
 81 shear localization zone to be able to change sides dynamically in the core depending on

82 how the normal stress evolves. We conclude that significant uncertainty remains regard-
83 ing how slip-induced pore pressure changes interact with the shear zone and/or fault core
84 and dynamically change the effective normal stress.

85 Here, we introduce a somewhat conservative and simplified view and select the av-
86 erage pore pressure through the shear zone as the relevant pore pressure for computing
87 the effective normal stress. We allow the shear zone to have a different permeability than
88 the host rock. This choice of the relevant pore pressure implies that the shear-zone width
89 is initially at steady state and not localizing or delocalizing at any relevant frictional or
90 diffusional time scale. As we explain in more detail in the next section, the problem of
91 selecting the appropriate pore pressure for shear of a finite-width fault zone in a poroe-
92 lastic medium remains largely unsolved and likely needs explicit modeling.

93 When sheared and perturbed, e.g., due to changes in slip speed, the fault gouge
94 can dilate or compact. The process changes the void volume fraction of the gouge, which
95 is also approximately the porosity of the gouge. If the volume change occurs faster than
96 the fluid pressure can equilibrate, then the changes in the void volume fraction can dra-
97 matically alter the pore pressure. Much like other processes of frictional interfaces, the
98 influence of these volume changes on frictional strength has not been derived from first
99 principles. The related models and theory have been largely derived and developed based
100 on empirical observations (e.g. Marone et al., 1990; Lockner & Byerlee, 1994; Proctor
101 et al., 2020). Nevertheless, the process can be understood as the result of continuous re-
102 arranging and deformation of grains in the gouge to accommodate sliding. Based on ex-
103 perimental results (Marone et al., 1990), Segall and Rice (1995) postulated, following the
104 critical state concept in soil mechanics, the existence of a steady-state void volume (or
105 porosity) which establishes itself eventually for sliding at steady state with a given con-
106 stant slip velocity. If the slip speed increases or decreases, the granular structure dilates
107 or compacts, respectively. Dilatancy and compaction are well established from labora-
108 tory frictional experiments spanning three decades (e.g. Marone et al., 1990; Lockner
109 & Byerlee, 1994; Proctor et al., 2020) and have been attributed to strain-rate harden-
110 ing of visco-plastic asperity contacts in simulations of rough interfaces (Hulikal et al.,
111 2018) as well as the dynamics of grains in simulations of granular media without viscoplas-
112 ticity (Ferdowsi & Rubin, 2020).

Segall and Rice (1995) used the laboratory observations of Marone et al. (1990), which documented porosity changes in a velocity-stepping experiment under drained conditions, to propose a model for the observed porosity changes. They postulated the existence of a steady-state porosity which depends on the slip velocity and to which the porosity evolves with slip:

$$\dot{\phi} = -\frac{V}{L} \left(\phi - \phi_0 - \gamma \log \left(\frac{V}{V_0} \right) \right), \quad (1)$$

113 where ϕ_0 is the steady-state porosity at the reference slip speed V_0 , L is the character-
 114 istic state evolution distance and γ is an empirical dilatancy coefficient. Segall and Rice
 115 (1995) also proposed a related dilatancy model in which the porosity depends on the fric-
 116 tional state variable that reflects the evolution of the sliding surface (here equation 33).
 117 Near steady-state sliding, the two models behave the same, but some differences occur
 118 away from the steady state. Recent experiments have suggested that a state-variable for-
 119 mulation may be more appropriate (Proctor et al., 2020). We emphasize that even though
 120 γ is referred to as a dilatancy coefficient, the formulations by Segall and Rice (1995) de-
 121 scribe both dilatancy and compaction, or alternatively void volume changes.

122 Segall and Rice (1995) then coupled the dilatancy model with a simple single-degree-
 123 of-freedom spring slider system and a membrane diffusion model (Rudnicki & Chen, 1988)
 124 and carried out a linearized stability analysis and numerical simulations. This work was
 125 revisited by Segall et al. (2010) who expanded previous work on the spring-slider sta-
 126 bility analysis and explored a more elaborate homogenous diffusion model. However, the
 127 main goal of Segall et al. (2010) was to explore dilatancy as a mechanism that can quench
 128 earthquake instability and generate slow slip. Models using dilatancy for stabilization
 129 have found agreement with observed behavior of subduction zone slow-slip events (e.g.,
 130 Segall et al., 2010; Liu, 2013; Dal Zilio et al., 2020). These models go beyond the spring-
 131 slider analysis and explore a rate-and-state fault with dilatancy coupled to an elastic con-
 132 tinuum. However, to date, dilatancy coupled to a poroelastic bulk, as we do here, has
 133 not been explored.

134 In this study, we formulate a closed system of equations and carry out a linearized
 135 stability analysis of a rate-and-state fault with dilatancy coupled to a poroelastic bulk.
 136 Further, we allow the shear zone to have different diffusivity from the bulk.

137 The paper starts by discussing the governing equations, boundary conditions, and
 138 various effects that may arise from frictional sliding and dilatancy or compaction in a

139 poroelastic solid. That section concludes by presenting solutions for stresses and pore
 140 pressures at the fault in a joint Fourier-Laplace transform domain. The following sec-
 141 tion derives various constitutive relationship for the shear layers and presents the rate-
 142 and-state friction law. The section concludes with the mathematical formulation of the
 143 linearized stability analysis. Finally, we present the results and derive several simple ap-
 144 proximations that characterize stability in certain limiting cases. The section concludes
 145 by comparing these approximations to the full solutions to the characteristic equation
 146 obtained through a standard root-finding algorithm.

147 **2 Problem statement and boundary conditions**

148 We consider two poroelastic half spaces with interface at $y = 0$ that are uniformly
 149 sliding past each other with slip rate V_0 across the interface which is spatially and tem-
 150 porally uniform. V_0 is small enough such that inertial effects and wave-mediated stress
 151 transfer can be ignored. The interface is at a uniform shear stress τ_0 and effective nor-
 152 mal stress σ_0 and thus friction coefficient $f_0 = \tau_0/\sigma_0$. The pore pressure p is also at
 153 equilibrium and spatially uniform. At time $t = 0$, this steady-state configuration is per-
 154 turbed by introducing a Fourier mode slip perturbation $\delta_x = e^{st+ikx}$, with the total slip
 155 for $t > 0$ being $V_0t + \delta_x$. This non-uniform (or heterogeneous) slip excites spatial vari-
 156 ation in slip speed, shear stress, pore-pressure, and normal stress.

157 The displacements u_i and pressure changes p relative to an equilibrium pressure
 158 state are governed four coupled partial differential equations. These are (e.g., Detour-
 159 nay & Cheng, 1995)

$$Gu_{i,kk} + \frac{G}{1-2\nu}u_{k,ki} = \alpha p_{,i} \quad (2)$$

160 and

$$\frac{1}{M}p_{,t} - \kappa p_{,kk} = -\alpha u_{k,kt}, \quad (3)$$

161 where u_i are displacements and we have assumed that body forces are negligible. The
 162 equations are presented in the index notation. Subscript ", t " indicates the partial deriva-
 163 tive with respect to time, subscript ", i " indicates the partial derivative with respect to
 164 the spatial coordinate i . Index $i = 1$ refers to the x axis, which lies in the fault plane.
 165 Index $i = 2$ refers to the y axis that is perpendicular to the fault plane. Finally, index

166 $i = 3$ corresponds to the z axis, but all fields will be assumed invariant in that direc-
 167 tion since we will conduct a plane-strain analysis. Repeated indices such as " kk " rep-
 168 resent sum over all spatial indices. Finally, the material parameters are denoted as fol-
 169 lows, G : shear modulus, ν : drained Poisson's ratio, α : Biot-Willis parameter, M : Biot
 170 modulus. Finally, κ is the mobility, which is defined as the ratio between the permeabil-
 171 ity and fluid viscosity. Later we shall replace some of these parameters with other poroe-
 172 lastic parameters for more compact and intuitive expressions. In Appendix A, we pro-
 173 vide expressions for converting between poroelastic parameters and Table A1 with im-
 174 portant fixed parameters.

175 Under the assumption of the plane strain, the four coupled equations above can
 176 be decoupled and written out in terms of displacement functions \mathcal{E} and \mathcal{S} derived by Verruijt
 177 (1971); McNamee and Gibson (1960), but see also Detournay and Cheng (1995) for a
 178 more pedagogical description. We follow the procedure outlined in the Appendix of Heimisson
 179 et al. (2019), but solve the system of equations for a more general set of boundary con-
 180 ditions:

$$\lim_{y \rightarrow 0^\pm} u_x^+ - u_x^- = \delta_x, \quad (4)$$

$$\lim_{y \rightarrow 0^\pm} u_y^+ - u_y^- = \delta_y, \quad (5)$$

$$\lim_{y \rightarrow \pm\infty} u_i^\pm = 0, \quad (6)$$

$$\lim_{y \rightarrow \pm\infty} p^\pm = 0, \quad (7)$$

$$\lim_{y \rightarrow 0^\pm} \sigma_{xy}^+ - \sigma_{xy}^- = 0, \quad (8)$$

$$\lim_{y \rightarrow 0^\pm} \sigma_{yy}^+ - \sigma_{yy}^- = 0, \quad (9)$$

181 where $+$ and $-$ superscripts refer to the $y > 0$ and $y < 0$ half-spaces respectively, and
 182 σ_{xy}^+ , σ_{xy}^- , σ_{yy}^+ , and σ_{yy}^- refer to the shear and normal perturbations in stress on top of
 183 the initial uniform values. We note that boundary conditions are applied at $y \rightarrow 0^\pm$,
 184 which contains a layer with thickness 2ϵ as shown in Figure 1. We assume that the layer
 185 is "thin" and can be treated through the boundary conditions at $y \rightarrow 0^\pm$. In other words,
 186 we require that $\epsilon \ll \lambda_{min}$, where λ_{min} is the smallest length-scale over which any phys-
 187 ical fields vary along the x axis. This can be regarded as a boundary layer approach where
 188 the outer solution treats the shear zone as a mathematical zero-thickness interface, but
 189 the inner solution treats it as having a finite thickness.

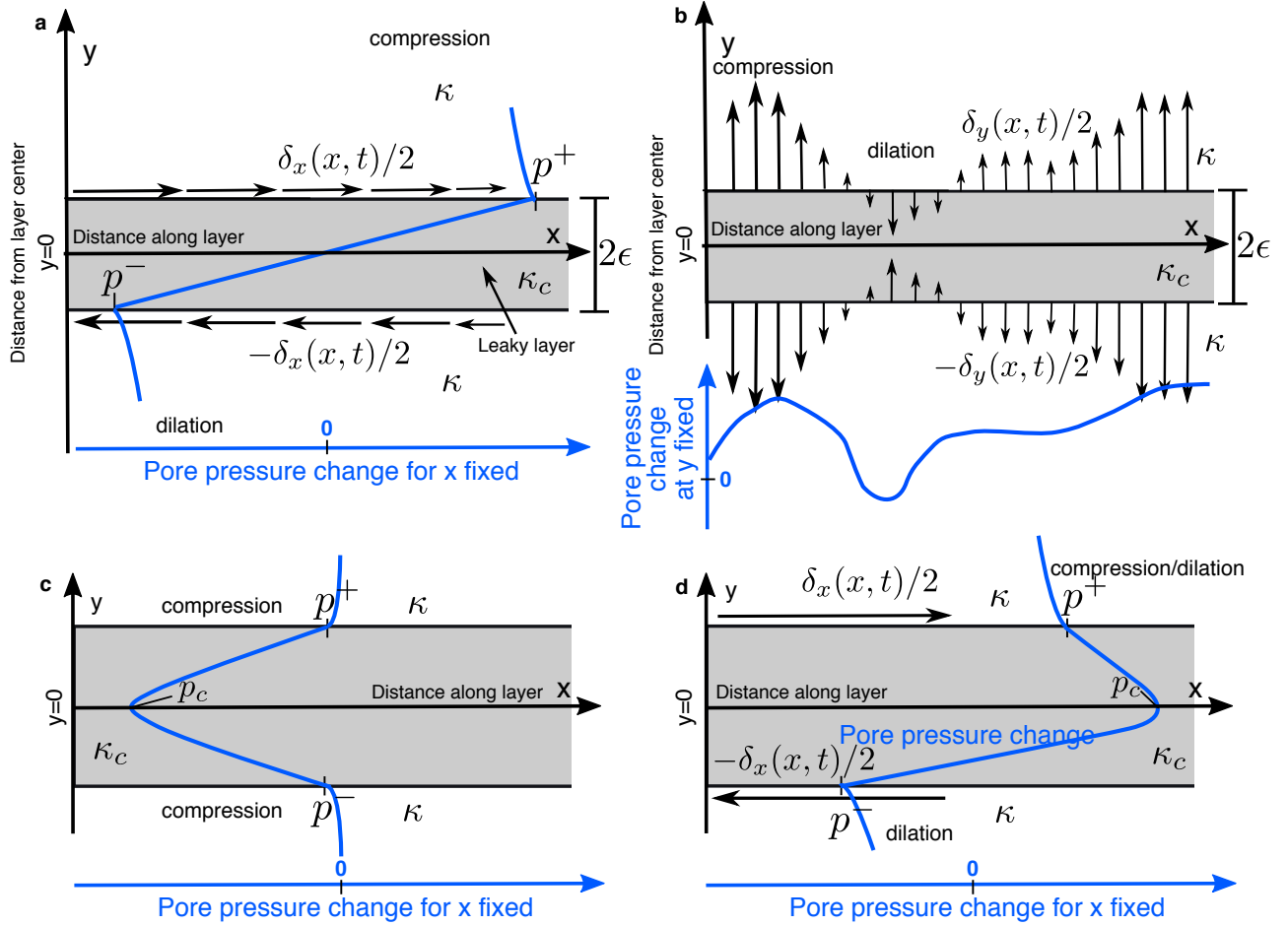


Figure 1. We explore various ways in which the deformation of a leaky and pressurized thin shearing layer of thickness 2ϵ and mobility κ_c , which we consider to be the shear zone, may couple to the surrounding poroelastic medium of mobility κ . **a** In-plane shear across the thin layer (indicated by horizontal arrows) compresses the bulk material on one side of the shear crack tip and dilates the material on the other. Due to poroelastic coupling, this increases pore pressure on the compressive side of the layer and decreases the pore pressure on the dilation side. This case, in which changes from pore pressure arise only from slip $\delta_x(x, t)$, was explored by Heimisson et al. (2019). **b** Processes in the thin layer, such as injection or inelastic dilation/compaction, may cause the layer to contract or expand (as indicated by vertical arrows), which would cause pore pressure changes in the surrounding medium. For example, expansion of the layer (outward facing arrows) would compress the the bulk (as indicated by the word "compression") and raise pore pressure in the bulk. **c** Internal pore pressure decrease can occur in the layer, $p_c(x, t) < 0$, perhaps due to inelastic dilation. The flow of pore fluids into the layer from the surrounding medium would cause compression adjacent to the layer in the bulk. **d** An example of a situation that combines changes in the pore pressure $p_c(x, t)$ in the layer (an increase in this case, e.g., due to fluid injection) and bulk effects of shear across the layer. The bulk material adjacent to the fault may undergo both compression and dilation (due to slip) and dilation due to pore pressure flow from the fault to the bulk if pressure $p_c(x, t)$ exceeds the slip induced pressure changes at the boundary, as shown.

190 The first two boundary conditions describe the deformation of the thin layer by ar-
 191 bitrary shearing, contraction, or expansion of the layer. The displacements discontinu-
 192 ities δ_x and δ_y across the layer are presented as occurring at the boundaries (Figure 1a-
 193 b). However, as long as the layer is thin, these displacements could be internal to the
 194 layer. For example $\delta_x(x, t)$ could both represent an infinitesimally thin slip surface within
 195 the layer (e.g., Heimisson et al., 2019), or it could represents a distributed shear through-
 196 out the layer.

197 The third and fourth boundary conditions guarantee that the displacements and
 198 pressure changes vanish at $y \rightarrow \pm\infty$. The fifth and sixth boundary conditions enforce
 199 that shear and normal stress are continuous across the layer. This condition also makes
 200 sense only for a thin layer.

201 Finally, we formulate a boundary condition for the pore pressure at the layer bound-
 202 ary. First, we recognize that this layer may generate pore pressure changes through sev-
 203 eral processes that may be slip-dependent, such as compaction or dilation (Segall & Rice,
 204 1995), chemical such as dehydration reactions, or simply due to applied perturbations
 205 from, for example, injection into the shear layer. Second, we recognize that such inter-
 206 face layers are generally produced by frictional wear, and such alterations may dramat-
 207 ically change the permeability (e.g. Caine et al., 1996; Wibberley & Shimamoto, 2003;
 208 Behnken & Faulkner, 2011). The difference in pore pressure at the boundary relative to
 209 the internal pore pressure determines the direction of the fluid flux. Taking $p_c(x, t)$ to
 210 be the pore pressure in the center of the layer (Figure 1 c-d), we can approximate the
 211 pressure gradient on the \pm sides of the layer as $(p^\pm - p_c)/\epsilon$. We use Darcy's law to pro-
 212 vide a flux boundary condition that equates the fluid flux out of each side of the layer
 213 to the flux into the bulk:

$$\left. \frac{dp^\pm}{dy} \right|_{y=0^\pm} = \pm \frac{\kappa_c}{\kappa} \frac{(p^\pm - p_c)}{\epsilon}, \quad (10)$$

214 where κ_c is the mobility within the shear layer. Equation (10) generalizes the leaky plane
 215 boundary condition of Song and Rudnicki (2017) and reduces to it if $p_c = 0$. Note that
 216 Equation (10) can result in an asymmetric flux out of the layer.

217 If we assume that equation (10) holds rigorously, then the pore pressure in the layer
 218 can be written as follows:

$$\begin{aligned}
 p(y) &= \frac{y}{\epsilon}(p^+ - p_c) + p_c & \text{if } 0 < y < \epsilon \\
 p(y) &= \frac{y}{\epsilon}(p_c - p^-) + p_c & \text{if } -\epsilon < y < 0.
 \end{aligned}
 \tag{11}$$

219 **2.1 Solutions to slip and pore pressure changes in Fourier-Laplace do-**
 220 **main: In-plane shear**

221 Let us define the joint Fourier-Laplace transform:

$$\bar{\bar{\delta}}_x(s, k) = \int_0^\infty \int_{-\infty}^\infty \delta_x(t, x) e^{-ikx-st} dx dt,
 \tag{12}$$

222 applied here to the slip $\delta_x(x, t)$, or displacement discontinuity across the layer in the x
 223 direction, where the bar symbol represents the Laplace transform in time and the hat
 224 represents the Fourier transform along the x spatial axis. Some symbols may not carry
 225 the hat symbol if they are explicitly written out in terms of wavenumber k .

226 Following the procedure outlined by Heimisson et al. (2019), we derive solutions
 227 for shear stress, pore pressure, and normal stress change at the slip surface ($y \rightarrow 0^\pm$)
 228 in the Fourier-Laplace domain. In the Laplace-Fourier transform domain. we obtain the
 229 following relationships between change in shear stress $\bar{\tau}'$, pore pressure change on either
 230 side of the layer \bar{p}^\pm , and change in total normal stress $\bar{\sigma}_{yy}$ in terms of $\bar{\bar{\delta}}_x$, $\bar{\bar{\delta}}_y$, and \bar{p}_c :

$$\bar{\tau}' = -\frac{G|k|\bar{\bar{\delta}}_x}{2(1-\nu_u)} \bar{H}_1(s, k)
 \tag{13}$$

231 and

$$\bar{p}^\pm = \mp \frac{ikGB\bar{\bar{\delta}}_x}{3} \frac{1+\nu_u}{1-\nu_u} \bar{H}_2(s, k) - \bar{p}_c \frac{\mathcal{F}}{\mathcal{F}+1} (\bar{H}_2(s, k) - 1) + \frac{|k|GB\bar{\bar{\delta}}_y}{3} \frac{1+\nu_u}{1-\nu_u} \bar{H}_2(s, k),
 \tag{14}$$

232 and

$$\bar{\sigma}_{yy} = \bar{p}_c \frac{2}{3B(1+\nu_u)} \frac{\mathcal{F}}{\mathcal{F}+1} (\bar{H}_1(s, k) - 1) - \frac{G|k|\bar{\bar{\delta}}_y}{2(1-\nu_u)} \bar{H}_1(s, k),
 \tag{15}$$

233 where

$$\bar{H}_1(s, k) = 1 - \frac{2(\nu_u - \nu)}{1 - \nu} \frac{ck^2}{s} \frac{1 + \mathcal{F}}{\mathcal{F} + \sqrt{1 + s/ck^2}} \left(\sqrt{1 + s/ck^2} - 1 \right),
 \tag{16}$$

234 and

$$\bar{H}_2(s, k) = \frac{\sqrt{1 + s/c k^2} - 1}{\sqrt{1 + s/c k^2} + \mathcal{F}}. \quad (17)$$

235 \mathcal{F} is a dimensionless group that characterizes the importance of flux across the fault:

$$\mathcal{F} = \frac{\kappa_c}{\kappa} \frac{1}{|k|\epsilon}. \quad (18)$$

236 **2.2 Solutions to slip and pore pressure changes in Fourier-Laplace do-**
 237 **main: Anti-plane shear**

238 Having solved the more complex in-plane shear problem, we may deduce the sim-
 239 pler anti-plane shear case. We note:

- 240 1. Any term of Eqs. (13), (14), and (15) that is linear in \bar{p}_c and $\bar{\delta}_y$ must be unchanged
 241 from the in-plane case, since these terms do not depend on fault-parallel slip.
- 242 2. Any term of Eqs. (13), (14), and (15) that is linear in $\bar{\delta}_x$ must be represented by
 243 the corresponding elastic anti-plane slip relationship, since anti-plane slip induces
 244 no volumetric stress and thus does not induce instantaneous or transient pore pres-
 245 sure response.

246 We thus arrive at the corresponding anti-plane shear relationships. We have:

$$\bar{\tau}' = -\frac{G|k|\bar{\delta}_x}{2}, \quad (19)$$

247 as was identified by Rice and Ruina (1983); Rice et al. (2001). Further, we find:

$$\bar{p}^{\pm} = -\bar{p}_c \frac{\mathcal{F}}{\mathcal{F} + 1} (\bar{H}_2(s, k) - 1) + \frac{|k|GB\bar{\delta}_y}{3} \frac{1 + \nu_u}{1 - \nu_u} \bar{H}_2(s, k) \quad (20)$$

248 and

$$\bar{\sigma}_{yy} = \bar{p}_c \frac{2}{3B(1 + \nu_u)} \frac{\mathcal{F}}{\mathcal{F} + 1} (\bar{H}_1(s, k) - 1) - \frac{G|k|\bar{\delta}_y}{2(1 - \nu_u)} \bar{H}_1(s, k), \quad (21)$$

249 where changes in normal stress σ_{yy} are identical to the in-plane case. It may seem sur-
 250 prising that the relationships above for anti-plane shear depend on Poisson's ratios (all

251 except (19), the slip to shear stress relationship). However, the terms with Poisson's ra-
 252 tio are not stress components that arise from sliding, but rather ones that result from
 253 pressurization of the layer and dilation/compaction of the layer. The terms that depend
 254 on δ_y represent mode I contribution of the interface deformation and terms with p_c rep-
 255 resent contributions from the pressure change at the interface. These contributions do
 256 not depend on the primary mode of sliding and are thus the same for the in-plane and
 257 anti-plane cases.

258 **3 Constitutive relations for a thin layer**

259 Here we describe the center pore pressure change p_c and the layer-perpendicular
 260 displacements δ_y in terms of the slip δ_x .

261 **3.1 Frictional constitutive law**

262 First, we consider the force balance within the layer:

$$\frac{\tau(x, t)}{\sigma(x, t) - p(x, y, t)} = f(x, y, t) \quad \text{for } -\epsilon < y < \epsilon, \quad (22)$$

263 where τ and σ are the shear stress and the effective normal stress in absence of pore pres-
 264 sure perturbations, respectively. Thus $\sigma = \sigma_0 + \sigma_{yy}$, where σ_0 is the total effective nor-
 265 mal stress at a equilibrium, meaning there are no perturbations present in stresses or pore-
 266 pressure. The effective normal stress is thus the difference between the total equilibrium
 267 normal stress and the ambient equilibrium pore-pressure, but these two scalars are al-
 268 ways combined in σ_0 the effective equilibrium normal stress. Similarly $\tau = \tau_0 + \tau'$ where
 269 τ_0 is the absolute equilibrium shear stress and τ' represents any perturbations in shear
 270 stress from slip, pore-pressure or from or external loading. The subscript $_0$ refers to a
 271 later assumption where we consider the system to be in equilibrium at $t = 0$ (see sec-
 272 tion 3.4).

273 We assume that τ and σ are constant with respect to y in the layer because the
 274 layer is thin. This assumption also implies that inertia can be ignored in the layer (Rice
 275 et al., 2014). f describes the frictional resistance at each point in the layer and p is the
 276 pore pressure perturbation assumed to follow the linear pressure distribution in equa-
 277 tion (11). In order to obtain the approximate frictional resistance of the entire layer, we
 278 average with respect to y using equation (11):

$$\tau \frac{(p_c - p^+) \log\left(\frac{\sigma - p^-}{\sigma - p_c}\right) + (p_c - p^-) \log\left(\frac{\sigma - p^+}{\sigma - p_c}\right)}{2(p_c - p^-)(p_c - p^+)} = \langle f \rangle, \quad (23)$$

279 where now all fields depend on x and t (not written explicitly for compactness), but not
 280 on y within the layer.

281 We assume that the layer-averaged fictional resistance is described by the rate-and-
 282 state friction law (e.g., Dieterich, 1979; Ruina, 1983; Marone, 1998):

$$\langle f \rangle = \frac{1}{2\epsilon} \int_{-\epsilon}^{\epsilon} f(x, y, t) dy = f_0 + a \log\left(\frac{V}{V_0}\right) + b \log\left(\frac{V_0 \theta}{L}\right), \quad (24)$$

283 where a is a constitutive parameter that weights the rate dependence of friction under
 284 constant state (also called the direct effect) and b is a constitutive parameter that weights
 285 the state dependence of friction at constant slip rate. L is the characteristics slip dis-
 286 tance over which the state θ evolves. A mathematical definition of θ is offered later in
 287 the section where we introduce the state evolution law. In order to maintain consistency
 288 with the linearized stability analysis, discussed and presented in section 3.4, we select
 289 the nominal coefficient of friction $f_0 = \tau_0/\sigma_0$ and the nominal slip speed as V_0 as the
 290 values at time $t = 0$, and the nominal state $\theta_0 = L/V_0$ as the steady-state value at
 291 time $t = 0$.

292 Equation (22) is non-linear, both in terms of strength dependence on pore-pressure
 293 and the coefficient of friction in equation (24). The linearization of the friction coeffi-
 294 cient is addressed in section 3.4. Here, we present the linearization with respect to changes
 295 in pore pressure (and assuming small changes in pore pressure), to provide a more in-
 296 tuitive expression than equation 23. The linearization renders:

$$\tau = \tau_0 + \tau'(t) = (\sigma_0 + \sigma_{yy}(t) - \langle p(t) \rangle) \left[f_0 + a \log\left(\frac{V}{V_0}\right) + b \log\left(\frac{V_0 \theta}{L}\right) \right], \quad (25)$$

297 where the relevant average pore pressure $\langle p \rangle$ in the layer can be written as:

$$\langle p \rangle = \frac{1}{2\epsilon} \int_{-\epsilon}^{\epsilon} p(y) dy = \frac{1}{2} \left(p_c + \frac{p^+ + p^-}{2} \right). \quad (26)$$

298 Hence we conclude that, given our assumptions, we can simply use the average pres-
 299 sure in the layer as the relevant pore pressure in computing the effective normal stress

300 in computing the shear resistance. As a reminder, our assumptions include the linear pore
 301 pressure distribution within the shear layer, the averaging of frictional strength described
 302 earlier in this section, and considering changes in pore pressure that are small compared
 303 to σ .

304 We note that the average pore pressure in the (distributed) shearing layer that we
 305 use in this study may not be a universally valid approach. In the presence of a thin low-
 306 permeability structure surrounding or next to the shearing layer, as typical for a fault
 307 core, the relevant pore pressure may be different (Jha & Juanes, 2014; Heimisson et al.,
 308 2019). Such structures are expected to be significant in well-developed fault zones (Caine
 309 et al., 1996). Our view could be most appropriate for less developed faults and labora-
 310 tory settings where the shear zone represents simulated gouge, or scenarios where the
 311 fault core may not generate a significant permeability contrast or flow barrier with the
 312 shear zone and/or the surrounding rock.

313 Furthermore, the localization of slip in fluid-saturated thin granular layers of dis-
 314 tributed shear is not fully understood at present and may require explicit modeling. If
 315 an ongoing localization process occurs, we also expect the relevant pore pressure to evolve
 316 in a complex way that requires explicit modeling. For example, studies indicate that, as
 317 instability develops, a localization process occurs and a distributed shear layer may col-
 318 lapse to a much narrower slip "surface" with the width of the order of several microns
 319 (Rice et al., 2014; Platt et al., 2014). We expect that the relevant effective normal stress
 320 for shear resistance would then be determined by the pore pressure over that localized
 321 shear surface.

322 Equation (25) requires an equation for the evolution of the state variable θ , for ex-
 323 ample, the aging law:

$$\frac{d\theta}{dt} = 1 - \frac{\theta V}{L} - \frac{\alpha_{LD}\theta}{b\sigma} \dot{\sigma} \quad (27)$$

324 or the slip law (Ruina, 1983) These state evolution laws are identical when linearized around
 325 steady state slip and our analysis encompasses both (see section 3.4). Here, we have in-
 326 cluded the correction of Linker and Dieterich (1992) for the dependence of state on nor-
 327 mal stress. This dependence is proportional to the empirical Linker and Dieterich (1992)
 328 constant α_{LD} , which is typically between 0 and 0.5, but always less than f_0 .

329

3.2 Constitutive equations for pore pressure in the layer

330

331

Now we derive an evolution equation for the average pore pressure in the layer. Following Segall and Rice (1995), the fluid mass conservation in the layer requires:

$$\frac{\partial m}{\partial t} + \frac{\partial q}{\partial y} = 0, \quad (28)$$

332

333

334

335

336

337

338

339

340

where m is the fluid mass content and q is the fluid mass flux. This expression considers the fluid mass flux along the layer (along x) to be negligible, which is valid if flux along y dominates over flux along x . One obvious example is if the mobility or permeability in y direction is much larger than in the x direction. However, we expect this to hold more generally since the flux along y is proportional to $1/\epsilon$ but the flux along x is proportional to k and $\epsilon k \ll 1 \Rightarrow k \ll 1/\epsilon$. Nevertheless, this also depends on the relation between the permeability of the host rock and permeability. If the host-rock is impermeable (or has low permeability compared to the one along the shear layer) then the flux along x cannot be ignored.

341

342

We write $m = \rho_f n$, where ρ_f is the fluid density and $n = n^e + n^p$ is the sum of the elastic and plastic void volumes. Taking the time derivative of m yields

$$\dot{m} = \dot{\rho}_f n + \rho_f \dot{n}. \quad (29)$$

343

344

345

346

347

348

349

350

351

352

353

354

355

356

We now propose linearized relationships for the elastic void compressibility $n^e = \phi(\beta_n^p \dot{p} - \beta_n^\sigma \dot{\sigma})$ and $\dot{\rho}_f = \rho_{fo}(\beta_f^p \dot{p} + \beta_f^\sigma \dot{\sigma})$, where β_f^p and β_n^p are fluid and elastic void compressibilities, respectively. Superscript p on β_f^p or β_n^p refers to ‘‘pressure’’ and specifies that this compressibility is defined under isotropic volumetric stress or pressure. Superscript σ on β_f^σ or β_n^σ refers to normal stress, specifically here σ_{yy} , and specifies that this compressibility is defined under uniaxial compressive or tensile stress. For example, for a linear elastic solid, $\beta^p = 1/K$, where K is the bulk modulus. However $\beta^\sigma = (1+\nu)/(3K(1-\nu))$, which is the so called P-wave modulus. For $\nu = 0.25$, we find $\beta^\sigma = 5\beta^p/9$. We assume that $\sigma > 0$ reflects increased compression, or the compression positive convention. Thus increased normal stress reduces the void-volume and decreases the fluid mass in each control volume. We refer the reader to Cocco and Rice (2002) for the detailed discussion of isotropic and uniaxial compressibilities in a poroelastic solid. The reference compressibilities are defined at the reference void fraction ϕ , which we interpret as porosity, and reference fluid density ρ_{fo} . Further, we assume that the plastic void fraction is

357 equal to the plastic porosity: $n^{pl} = \phi^{pl}$, where the superscript "pl" refers to "plastic".

358 Thus, we arrive at:

$$\dot{m} = \rho_{fo}\phi(\beta_f^p\dot{p} + \beta_f^\sigma\dot{\sigma}) + \rho_{fo}\phi(\beta_n^p\dot{p} - \beta_n^\sigma\dot{\sigma} + \dot{\phi}^{pl}/\phi). \quad (30)$$

359 Combining equations (28) and (30) and integrating over the shear layer yields:

$$2\epsilon\rho_{fo}\phi \left[(\beta_f^p + \beta_n^p)\langle\dot{p}\rangle + (\beta_f^\sigma - \beta_n^\sigma)\dot{\sigma} + \langle\dot{\phi}\rangle^{pl}/\phi \right] + q^+ - q^- = 0, \quad (31)$$

360 Inserting the expressions for the fluid mass flux given a linear pressure distribution (equa-
361 tions (10) and (11)) provides:

$$\langle\dot{p}\rangle + \frac{\beta_f^\sigma - \beta_n^\sigma}{\beta_f^p + \beta_n^p}\dot{\sigma} = -\frac{\langle\dot{\phi}\rangle^{pl}}{\phi(\beta_f^p + \beta_n^p)} + \frac{\kappa_c}{\epsilon^2\phi(\beta_f^p + \beta_n^p)}\left(\frac{1}{2}(p^+ + p^-) - p_c\right). \quad (32)$$

362 We have thus arrived at an evolution equation that relates normal stress (constant
363 over the layer) with average pore pressure and dilatancy, where the source of pore pres-
364 sure stems from inelastic changes in porosity ϕ^{pl} . Segall and Rice (1995) and Segall et
365 al. (2010) proposed that the inelastic porosity is a function of the state $\phi^{pl}(\theta)$. This idea
366 has been further observationally supported by Proctor et al. (2020). We assume that the
367 state variable description of the plastic porosity changes reflects the average porosity change
368 in the shear layer:

$$\langle\phi\rangle^{pl} = \phi_0 - \gamma \log\left(\frac{V_0\theta}{L}\right), \quad (33)$$

369 where γ is a dilatancy coefficient usually taken as $\gamma \sim 10^{-4}$. The rate of change of the
370 inelastic porosity is then given by:

$$\langle\dot{\phi}\rangle^{pl} = -\frac{\gamma}{\theta}\dot{\theta}. \quad (34)$$

371 **3.3 Fault-normal displacements of the shear layer**

372 We now seek a relationship that describes fault normal expansion or contraction
373 of a thin gouge layer $\delta_y = u_y(y = \epsilon) - u_y(y = -\epsilon)$. We start by stating the conserva-
374 tion of gouge mass, m_g , per unit volume:

$$\frac{\partial m_g}{\partial t} + \frac{\partial}{\partial y} ((1-n)\rho_g \dot{u}_y) + \frac{\partial}{\partial x} ((1-n)\rho_g \dot{u}_x) = 0, \quad (35)$$

375 where ρ_g is the gouge density; note that this is not the bulk density but the density of
 376 non-porous and intact gouge mass, that is the solid constituent of the gouge with all pores
 377 removed. Deformation u_x and u_y here refer to the internal deformation field of the gouge.
 378 Now $m_g = (1-n)\rho_g$ and thus:

$$\dot{m}_g = -\rho_g \dot{n} + (1-n)\dot{\rho}_g. \quad (36)$$

379 Following the same arguments as in the previous section, we arrive at a linearized rela-
 380 tionship:

$$\dot{m}_g \approx -\rho_{g0}\phi(\beta_n^p \dot{p} - \beta_n^\sigma \dot{\sigma} + \dot{\phi}^{pl}/\phi) + (1-\phi)\rho_{g0}(\beta_g^p \dot{p} + \beta_g^\sigma \dot{\sigma}), \quad (37)$$

381 where now β_g is the compressibility of the intact and non-porous gouge material and again
 382 superscript p and σ refer to the isotropic and uniaxial compressibilities, respectively.

383 Inserting Eq. 37 in Eq. 35 and integrating over the shear layer provides a relation-
 384 ship between dilatancy, pressure, and normal stress changes and gouge fault normal dis-
 385 placements:

$$\dot{\delta}_y = 2\epsilon \left(\frac{\phi}{1-\phi} \beta_n^p - \beta_g^p \right) \left[\langle \dot{p} \rangle - \frac{\left(\frac{\phi}{1-\phi} \beta_n^\sigma + \beta_g^\sigma \right)}{\left(\frac{\phi}{1-\phi} \beta_n^p - \beta_g^p \right)} \dot{\sigma} \right] + 2\epsilon \frac{\langle \dot{\phi} \rangle^{pl}}{1-\phi}. \quad (38)$$

386 If we assume that, at time $t = 0$, the fault is in a pressure equilibrium and sliding at
 387 steady state, the equation can be integrated trivially:

$$\delta_y = 2\epsilon \left(\frac{\phi}{1-\phi} \beta_n^p - \beta_g^p \right) \left[\langle p \rangle - \frac{\left(\frac{\phi}{1-\phi} \beta_n^\sigma + \beta_g^\sigma \right)}{\left(\frac{\phi}{1-\phi} \beta_n^p - \beta_g^p \right)} \sigma \right] + 2\epsilon \frac{\langle \phi \rangle^{pl}}{1-\phi}. \quad (39)$$

388 Where we have assumed that the average of \dot{u}_x with respect to y over the layer thick-
 389 ness is zero such that the x flux term in equation (35) is essentially neglected. This may
 390 be justified by assuming that internal deformation of the shear layer with respect to $y =$
 391 0 is symmetric. This is likely if one side of the fault slips the same amount as the other,
 392 which is usually the case for symmetric geometries. We entrust the analysis of what might
 393 occur if such symmetry is not present to future work.

394

3.4 Linearized stability analysis

395

396

397

398

399

400

401

402

403

We now seek to analyze the stability of the steady shear (or sliding) in the layer to small perturbations. If the perturbation is small, the friction law and other constitutive relationship can be linearized around the initial steady-state configuration. We seek a solution to the linearized form (Rice et al., 2001) of the friction law and state evolution (Eqs. 25 and 27, respectively) as well as the linearized equation describing the time-evolution of the layer pressure p_c (Eq. 32). We carry out the stability analysis in the joint Laplace-Fourier transform domain (Eq. 12), which is equivalent to seeking a solution to the linearized system of equation for a slip perturbation $\delta_x = e^{st+ikx}$, which is applied at $t = 0$ (e.g., Rice et al., 2001).

404

405

406

407

408

The goal of the linearized stability analysis is to obtain the characteristic equation where we can solve for s as a function of k and other parameters. If the solution has $\Re(s(k)) > 0$, then the steady-state sliding is linearly unstable to the perturbations with corresponding wavenumbers, whereas if $\Re(s(k)) < 0$, the sliding is stable and the perturbations decay exponentially.

409

410

411

412

413

414

We note that the sign of k when it refers to a Fourier-mode perturbation in slip applied to the fault simply reflects the direction of the slip wave as it travels along the interface. The symmetry of the problem indicates that there is no inherent dependence on the wave directionality. Indeed, the term with the opposite sign in p^+ and p^- (equation 14), which implies the directionality dependence (as was discussed by Heimisson et al. (2019)), cancels when computing $\langle p \rangle$.

415

416

The linearized form of Eqs. 25 and 27 around steady state sliding can be expressed (Rice et al., 2001):

$$\frac{d}{dt}\tau'(t) = -\frac{a\sigma_0}{V_0}\frac{dV}{dt}(f_0 - \alpha_{LD})\frac{d}{dt}(\sigma_{yy} + p) - \frac{V_0}{L}\left[\tau_0 + \tau'(t) - f_0(\sigma_0 - \sigma_{yy} - p) - \frac{(a-b)\sigma_0}{V_0}(V - V_0)\right], \quad (40)$$

417

Transforming in the Laplace-Fourier domain renders (Heimisson et al., 2019):

$$\left(s + \frac{V_0}{L}\right)\bar{\tau}' = -\left[f_0\left(s + \frac{V_0}{L}\right) - \alpha_{LD}s\right](\bar{\sigma}_{yy} + \bar{p}) + \left[\frac{a\sigma_0}{V_0}s^2 + \frac{(a-b)\sigma_0}{L}s\right]\bar{\delta}_x. \quad (41)$$

418 Expressions for $\bar{\tau}'$ and $\bar{\sigma}_{yy}$ are provided in Eqs 13 and 15, but we note the introduction
 419 of the minus sign in front of $\bar{\sigma}_{yy}$ due to a change in sign convention since the equation
 420 describing friction considers tensile stress to be negative. As previously discussed, the
 421 value chosen for the relevant pore pressure within the layer is open to some interpreta-
 422 tion but here we take the average value as in Eq. 26.

423 Now we seek to eliminate the eigenfunction $\bar{\delta}_x$ from the equation above and retrieve
 424 the characteristic equation. However, we first need to derive linear relationships such that
 425 $\bar{p}_c \propto \bar{\delta}_x$ and $\bar{\delta}_y \propto \bar{\delta}_x$.

426 Let $\phi^{pl} = \phi_0 + \Delta\phi_p$, $\theta = L/V_0 + \Delta\theta$, and $V = V_0 + \Delta V$ where Δ indicates a small
 427 perturbation around the steady state value, which is the first term on the right hand side
 428 of each equation. Inserting into Eq. 34 and carrying out a linearization around steady
 429 state provides the following expression for $\dot{\phi}^{pl}$ and the corresponding Laplace transform

$$\Delta\dot{\phi}^{pl} = -\frac{\gamma V_0}{L}\Delta\dot{\theta} \Rightarrow \mathcal{L}(\Delta\dot{\phi}^{pl}) = \overline{\Delta\dot{\phi}^{pl}} = -\frac{\gamma V_0 s}{L}\overline{\Delta\theta}. \quad (42)$$

430 From Segall and Rice (1995), we have a linearized state evolution law:

$$\Delta\dot{\theta} = -\frac{V_0}{L}\Delta\theta - \frac{\Delta V}{V_0} \quad (43)$$

431 and the Laplace transform renders

$$\overline{\Delta\theta} = -\frac{s\bar{\delta}_x}{V_0(s + \frac{V_0}{L})}. \quad (44)$$

432 Thus the linear relationship between plastic changes in porosity (or alternatively inelas-
 433 tic dilatancy or compaction) is

$$\langle \bar{\phi} \rangle^{pl} = \frac{\gamma}{L} \frac{s\bar{\delta}_x}{(s + \frac{V_0}{L})}, \quad (45)$$

434 where we interpret the relationship as the average representing the plastic changes in poros-
 435 ity within the shear zone.

436 Applying the Laplace transform to Eq. 32 and substituting Eq 45 yields

$$\langle \bar{p} \rangle = \frac{1}{2} \left(\bar{p}_c + \frac{\bar{p}^+ + \bar{p}^-}{2} \right) = -\frac{\gamma}{\beta L} \frac{s}{s + \frac{V_0}{L}} \bar{\delta}_x + \frac{\kappa_c}{2\beta\epsilon^2 s} (\bar{p}^+ - 2\bar{p}_c + \bar{p}^-), \quad (46)$$

437 Further substitution of Eq. 14 then provides one linear relationship between \bar{p}_c , $\bar{\delta}_y$, and
 438 $\bar{\delta}_x$. However, another constitutive relationship is needed to eliminate both \bar{p}_c and $\bar{\delta}_y$. This
 439 relationship comes from Eq. 39 by taking the Laplace transform and substituting Eq.
 440 45:

$$\bar{\delta}_y = 2\epsilon \left(\frac{\phi}{1-\phi} \beta_n^p - \beta_g^p \right) \left[\frac{1}{2} \left(\bar{p}_c + \frac{\bar{p}^+ + \bar{p}^-}{2} \right) - \frac{\left(\frac{\phi}{1-\phi} \beta_n^\sigma + \beta_g^\sigma \right)}{\left(\frac{\phi}{1-\phi} \beta_n^p - \beta_g^p \right)} \bar{\sigma}_{yy} \right] + \frac{2\epsilon}{1-\phi} \frac{\gamma}{L} \frac{s \bar{\delta}_x}{\left(s + \frac{V_0}{L} \right)}. \quad (47)$$

441 Then through substitution of Eqs. 14 and 15 for the in-plane case, or Eqs. 20 and 21 for
 442 the anti-plane case, we obtain another linear relationship between \bar{p}_c , $\bar{\delta}_y$, and $\bar{\delta}_x$.

443 This means that the linear relationship between stress or pore pressure and \bar{p}_c , $\bar{\delta}_y$,
 444 and $\bar{\delta}_x$ in Eqs. 13, 14, and 15 for in-plane, or Eqs. 19, 20, and 21 for anti-plane can all
 445 be expressed only in terms of $\bar{\delta}_x$. Then substitutions of those expressions into the char-
 446 acteristic equation (41) allows for elimination of $\bar{\delta}_x$ and provides finally two equations
 447 that can be solved numerically for $s(k)$. The two equations are obtained by requiring that
 448 both the real part and imaginary part of the characteristic equation are zero (e.g., Rice
 449 et al., 2001; Heimisson et al., 2019). We do not present here the full characteristic equa-
 450 tion due to the complexity of the expression, but provide a Matlab code where it is im-
 451 plemented and can be solved (see Acknowledgments). In the next section, we discuss some
 452 approximation and implications as well as show numerical solutions.

433 4 Results

454 Let us present the results on the stability of steady-state sliding of a dilating shear
 455 layer embedded into and coupled with a poroelastic solid. Much of this discussion fo-
 456 cuses either on approximate expressions for the critical wavenumber, or solving the char-
 457 acteristic equation numerically using a standard root finding algorithm.

458 The critical wavenumber $k_{cr} = 2\pi/\lambda_{cr}$ represents the wavenumber at the bound-
 459 ary between stable and unstable sliding. The critical wavenumber marks the point of a
 460 Hopf bifucation where $\text{Re}(s(k_{cr})) = 0$ but $\text{Im}(s(k_{cr})) \neq 0$ in general. A small-magnitude
 461 perturbation in slip with a larger wavenumber ($k > k_{cr}$), or alternatively a smaller wave-
 462 length, would decay exponentially. However, a perturbation in slip of a smaller wavenum-
 463 ber than k_{cr} ($k < k_{cr}$), or alternatively larger wavelength, would grow and may nucle-

464 ate a seismic event. A Fourier-mode perturbation with exactly $k = k_{cr}$ would simply
 465 oscillate with a fixed frequency and neither grow nor decay.

466 In the following sections, we present approximations to the critical wavenumber in
 467 certain limiting cases. To obtain these approximate expressions, we carry out following
 468 steps.

- 469 1. We introduce s' and k' , which are non-dimensional versions of s and k and are ob-
 470 tained by substitution $s = s'V_0/L$ and $k = k'k_{cr}^{anti}$, where $k_{cr}^{anti} = 2\sigma_0(b-a)/(GL)$
 471 is the critical wavenumber for quasi-static, anti-plane sliding between two elastic
 472 solids (Rice et al., 2001). This quantity is of the same order as the correspond-
 473 ing in-plane sliding wavenumber (Rice et al., 2001) but does not depend on Pois-
 474 son's ratio, which can be either drained or undrained. This non-dimensionalization
 475 implies that s' and k' are generally of order unity near critical stability.
- 476 2. We introduce a non-dimensional half-thickness ϵ' of the shear layer, by substitui-
 477 tion $\epsilon = \epsilon'/k_{cr}^{anti}$. Since a fundamental assumption of the analysis is that $k\epsilon \ll$
 478 1, we may use ϵ' as a small parameter in which the characteristic equation can be
 479 expanded.
- 480 3. We carry out a Taylor expansion of both the real and imaginary parts of the char-
 481 acteristic equation. We retain terms up to first order in ϵ' . We also explore the
 482 leading-order terms that are proportional to $1/\kappa_c$ if appropriate. These terms are
 483 retained because they become large if κ_c is small and thus may provide insight into
 484 transitional regimes at low shear-zone mobility.

485 4.1 Characteristic time scales

486 In order to obtain insight into the role of diffusion in the stability of the frictional
 487 interface, we start by analyzing the time scales involved as perturbations grow around
 488 steady state sliding. The problem has three characteristic time scales. First, a frictional
 489 nucleation time scale:

$$t_{nu} = \frac{L}{V_0}, \quad (48)$$

490 which is a natural time-scale for the evolution of the frictional state and scales how fast
 491 instabilities nucleate or decay back to steady state sliding in a stable regime. Further,

492 it offers a first-order approximation to the instability time of sources above steady state
 493 in the spring-slider analysis (Heimissson & Segall, 2018).

Second, we investigate the time scale of diffusion into the bulk:

$$t_b = \frac{1}{ck^2}, \quad (49)$$

lastly, a time scale of flux in the shear layer:

$$t_f = \frac{1}{\mathcal{F}^2 ck^2} = \frac{\kappa^2 \epsilon^2}{\kappa_c^2 c} = \frac{c\epsilon^2}{M^2 \kappa_c^2}, \quad (50)$$

494 where the last equality is obtained by the substitution $\kappa = c/M$, which is the relation-
 495 ship between the mobility and hydraulic diffusivity in a linear poroelastic bulk.

From these time scales, we identify two non-dimensional time scales. First,

$$\mathcal{T}_f = \frac{t_{nu}}{t_f} = \frac{LM^2 \kappa_c^2}{V_0 c \epsilon^2}, \quad (51)$$

496 where \mathcal{T}_f represents the ratio of the time scale of nucleation to the time scale of flux through
 497 the shear layer. If \mathcal{T}_f is small compared to unity then nucleation occurs much faster than
 498 the fluid flux in the shear layer. Since such flux is needed to minimize the effects of di-
 499 lational stabilization, we expect that a small value of \mathcal{T}_f corresponds to the limit where
 500 dilatancy is important. On the other hand, if \mathcal{T}_f is large, then nucleation occurs over a
 501 longer time than the flux and dilatancy can be ignored.

502 The second non-dimensional time scale is $t_{nu}/t_b = Lck^2/V_0$, however, we substi-
 503 tute $k \rightarrow k_{cr}^{anti}$ since it is not convenient to express the non-dimensional time scale ex-
 504 plicitly in terms of k , which is treated as a variable in the characteristic equation. We
 505 thus obtain a non-dimensional time scale independent of k :

$$\mathcal{T}_b = \frac{4c\sigma_0^2(b-a)^2}{V_0 G^2 L}, \quad (52)$$

506 which is valid as long as the critical wavenumber is of the same order as k_{cr}^{anti} . When
 507 \mathcal{T}_b is small compared to unity we may effectively ignore the fluid diffusion in the bulk
 508 on the time scale of nucleation and we expect undrained bulk response. However, if \mathcal{T}_b
 509 is large then fluid in the bulk can diffuse at the time scale of nucleation and the bulk re-
 510 sponse is drained. For $\mathcal{T}_b \sim 1$, we expect transient poroelastic response of the bulk.

511 The two non-dimensional time scales here share several parameters, notably the
 512 hydraulic diffusivity of the host rock c . Moving forward, we shall investigate different

513 limits of stability by systematically changing either \mathcal{T}_f or \mathcal{T}_b while keeping the other pa-
 514 rameter constant.

515 4.2 Limit of $\kappa_c \rightarrow 0$

516 Let us analyze a simple limit where the permeability or mobility of the shear layer
 517 is zero, in addition to assuming that the bulk response is either drained or undrained.
 518 In this limit, as $\epsilon \rightarrow 0$, one can show, for in-plane sliding, that:

$$|k_{cr}| \simeq k_{cr}^{un} \left(1 - \frac{f_0 \gamma}{\beta \sigma_0 (b-a)} + \mathcal{O}(\epsilon) \right), \quad (53)$$

519 where

$$k_{cr}^{un} = k_{cr}^{anti} (1 - \nu_u) = \frac{2\sigma_0 (b-a)(1 - \nu_u)}{GL} \quad (54)$$

520 is the critical wavenumber for the corresponding elastic problem of in-plane sliding as-
 521 suming an undrained Poisson's ratio. We present k_{cr} within an absolute value to reflect
 522 that it can be both positive and negative depending on the directionality of the slip wave
 523 as was previously discussed. This also implies that, if the right hand side of the equaion
 524 is negative, then clearly the critical wavenumber does not exist.

525 Similarly, for drained bulk response

$$|k_{cr}| \simeq k_{cr}^d \left(1 - \frac{f_0 \gamma}{\beta \sigma_0 (b-a)} + \mathcal{O}(\epsilon) \right), \quad (55)$$

526 where

$$k_{cr}^d = k_{cr}^{anti} (1 - \nu) = \frac{2\sigma_0 (b-a)(1 - \nu)}{GL} \quad (56)$$

527 is similarly the drained elastic critical wavenumber of in-plane sliding.

528 For anti-plane sliding, there is no difference in the bulk response at drained or undrained
 529 condition (to zeroth order in ϵ') and the corresponding limit is simply

$$|k_{cr}| \simeq k_{cr}^{anti} \left(1 - \frac{f_0 \gamma}{\beta \sigma_0 (b-a)} + \mathcal{O}(\epsilon) \right), \quad (57)$$

530 We thus observe that the dilatancy has a primary effect on the critical wavenum-
 531 ber in this limit. Equations (53) and (57) are, in a sense, equivalent to the undrained
 532 limit identified by Segall and Rice (1995) with a single-degree-of-freedom spring-slider
 533 analysis, except equations (53) and (57) are for a deformable poroelastic bulk. However,
 534 equation (55) does not have a direct correspondence in the Segall and Rice (1995) anal-
 535 ysis. This is because the Segall and Rice (1995) analysis had effectively only one diffu-
 536 sion time controlled by the hydraulic diffusivity c of the bulk. Here, we consider that the
 537 time scale of flux within the shear layer may be very different (see Section 4.1). Thus
 538 this analysis adds to the findings of Segall and Rice (1995) by suggesting that, as long
 539 as the shear layer is sufficiently impermeable, then dilatancy stabilization can occur even
 540 in a highly diffusive surroundings.

541 The first-order correction for Eqs. (53) and (55) can be written out explicitly as:

$$\mathcal{O}(\epsilon) = \epsilon \frac{2f_0\gamma(f_0\gamma - (b-a)\phi\sigma_0(\beta_f^p + \beta_n^p))(\beta_g^p + \phi(\beta_f^p - \beta_g^p))(\beta_f^p - \beta_f^\sigma + \beta_n^p + \beta_n^\sigma)}{L\phi^2\sigma_0(\beta_f^p + \beta_n^p)^3(b-a)(1-\phi)}. \quad (58)$$

542 The corresponding anti-plane $\mathcal{O}(\epsilon)$ correction term in equation (57) is obtained by mul-
 543 tiplying the in-plane correction (equation 58) by $1/(1-\nu)$ and $1/(1-\nu_u)$ for the drained
 544 and undrained bulk responses, respectively.

545 This correction arises due to the shear-zone expansion from non-elastic porosity
 546 changes from dilatancy and elastic porosity changes due to pore pressure change and nor-
 547 mal stress changes. It is likely that the sign of this term is mostly governed by the sign
 548 of $f_0\gamma - (b-a)\phi\sigma_0(\beta_f^p + \beta_n^p) = f_0\gamma - (b-a)\sigma_0\beta$. Thus, if $f_0\gamma/((b-a)\sigma_0\beta) > 1$, this term
 549 would act to destabilize. However, $f_0\gamma/((b-a)\sigma_0\beta) = 1$ is the condition when Eqs.
 550 (53), (55), and (57) suggest no unstable wavenumbers, since $k_c = 0$ to the leading or-
 551 der. We thus conclude that, for sets of parameters where the interface is conditionally
 552 unstable due to small perturbations around steady state, fault-perpendicular displace-
 553 ments act to further stabilize sliding as $\kappa_c \rightarrow 0$.

554 4.3 Undrained bulk response ($c \rightarrow 0$)

555 In this particular limit, we neglect any diffusion of fluids in the bulk. However, we
 556 note that the shearing layer itself can equilibrate pore pressure, in other words, $\kappa_c >$
 557 0. In this particular case, the characteristic equation is greatly simplified because $\bar{H}_1 \rightarrow$

558 1 and $\bar{H}_2 \rightarrow 1$ by design (Heimisson et al., 2019). However the full solution to the sys-
 559 tem is still too complicated provide any useful insight if written out as an equation. We
 560 thus approximate the characteristic equation following the procedure outlined before.
 561 We obtain the following expression:

$$|k_{cr}| \simeq k_{cr}^{un} \frac{1}{1 + \mathcal{C}}, \quad (59)$$

562 where \mathcal{C} is a non-dimensional and non-negative parameter:

$$\mathcal{C} = \epsilon \frac{2f_0\gamma(3 - 2B(1 + \nu_u))}{3L(1 - \phi)} \quad (60)$$

563 The corresponding anti-plane limit is obtained by substitution of $k_{cr}^{un} \rightarrow k_{cr}^{anti}$ and
 564 $\mathcal{C} \rightarrow \mathcal{C}/(1 - \nu_u)$.

565 In the limit $\epsilon \rightarrow 0$, we clearly see that $k_{cr} = k_{cr}^{un}$ as is expected. It is notable that
 566 \mathcal{C} describes stabilization due to expansion of the gouge in response to inelastic dilatancy,
 567 which causes fault perpendicular displacements. The bracket $3 - 2B(1 + \nu_u) \geq 0$, since
 568 at most $B = 1$ and $\nu_u = 0.5$. This bracket characterizes the competition between two
 569 processes: increased compression of the shear layer due to expansion against the poroe-
 570 lastic host rock and increased pore pressure in the shear layer due to the compression
 571 of the host rock. If $B = 1$, and the undrained Poisson's ratio of the host rock implies
 572 that it is nearly incompressible, the two effects cancel completely. We conclude that the
 573 influence of the shear layer expansion in the undrained bulk limit can be neglected as
 574 long as

$$\mathcal{C} = \epsilon \frac{2f_0\gamma(3 - 2B(1 + \nu_u))}{3L(1 - \phi)} \ll 1. \quad (61)$$

575 It is worth noting that higher order terms may become significant in the limit of
 576 $\kappa_c \rightarrow 0$. But, as we recognize in the previous section, the limit of $\kappa_c = 0$ gives rise to
 577 dilatancy stabilization of the zeroth order with respect to ϵ . By retaining the leading-
 578 order terms with dependence on $1/\kappa_c$, we find that, in order for equation (60) to be a
 579 valid approximation, one needs to have:

$$\epsilon^4 \frac{V_0^2 \beta f_0 \gamma}{4L^2 \kappa_c^2 a \sigma_0} \ll 1. \quad (62)$$

580 If the inequality is violated, we expect the onset of stabilization through dilatancy in the
 581 sense identified by Segall and Rice (1995).

582 4.4 Drained bulk response ($c \rightarrow \infty$)

583 In this limit, we assume that the bulk is highly diffusive on any time scale relevant
 584 dilatancy and for the onset of instability. However, we assume that the shear layer pres-
 585 sure equilibrates on a finite time scale, i.e. $\kappa_c > 0$. We carry out the same procedure
 586 as for undrained bulk response to obtain an approximate expression for the critical wavenum-
 587 ber:

$$|k_{cr}| \simeq k_{cr}^d \frac{1}{1 + \mathcal{C}_d}. \quad (63)$$

588 Curiously, this approximation has exactly the same form as for the undrained bulk with
 589 some slight changes:

$$k_{cr}^d = \frac{2\sigma_0(b-a)(1-\nu)}{GL} \quad (64)$$

590 and

$$\mathcal{C}_d = \epsilon \frac{2f_0\gamma}{L(1-\phi)}. \quad (65)$$

591 The corresponding anti-plane limit is obtained by substitution of $k_{cr}^d \rightarrow k_{cr}^{anti}$ and
 592 $\mathcal{C}_d \rightarrow \mathcal{C}_d/(1-\nu)$.

593 The critical wavenumber for the undrained bulk response (Eq. 59) can be turned
 594 into the one for the drained bulk response (Eq. 63) simply by substituting $\nu_u \rightarrow \nu$ and
 595 setting $B = 0$. The substitution of the undrained Poisson's ratio by the drained one
 596 is obviously relevant. The substitution of $B = 0$ is also easily explained since, for the
 597 fully drained bulk response, fault perpendicular movements do not induce an increased
 598 pore pressure adjacent to the shear zone.

599 It is worth noting that the only compressibility that shows up in Eq. 59 and Eq.
 600 63 is $\beta = \phi(\beta_f^p + \beta_n^p)$ (defined in the same way as by (Segall & Rice, 1995)). All other
 601 compressibilities, such as those related to uniaxial compression or the fault gouge com-

602 compressibilities, influence the solution through higher-order terms that are neglected here,
 603 which indicates that the other compressibilities are not as important.

604 In the drained bulk limit, a violation of inequality (62) also indicates the onset of
 605 traditional dilatancy stabilization as in Segall and Rice (1995).

606 **4.5 Visualization of the characteristic equation**

607 Let us solve the characteristic equation using a standard root-finding algorithm.
 608 We focus on two parameter regimes for bulk and poroelastic properties: a generic gran-
 609 ite with $B = 0.6$, $\nu = 0.2$, $\nu_u = 0.4$ and a generic sandstone with $B = 0.85$, $\nu = 0.25$,
 610 and $\nu_u = 0.34$. Granites typically have a substantial difference in the drained and undrained
 611 Poisson's ratios and a Skempton's coefficient of about $B = 0.6$. Sandstones typically
 612 have a smaller difference between the drained and undrained Poisson's ratios and a large
 613 B near 1. These values are based on the poroelastic material parameters for rocks listed
 614 in Detournay and Cheng (1995) (see also references therein).

615 In addition to exploring the generic granite and sandstone cases, we also explore
 616 two limits - a thinner shear layer with $\epsilon = 1$ mm and a thicker shear layer with $\epsilon = 10$
 617 cm - which would reveal differences corresponding to the fault-normal displacement sta-
 618 bilization process. Other chosen parameters are listed in the Appendix (table A1).

619 **5 In-plane shear**

620 We first investigate the case of in-plane sliding which gives rise to more variabil-
 621 ity in the drained and undrained limits and better highlights the different regimes pre-
 622 viously discussed.

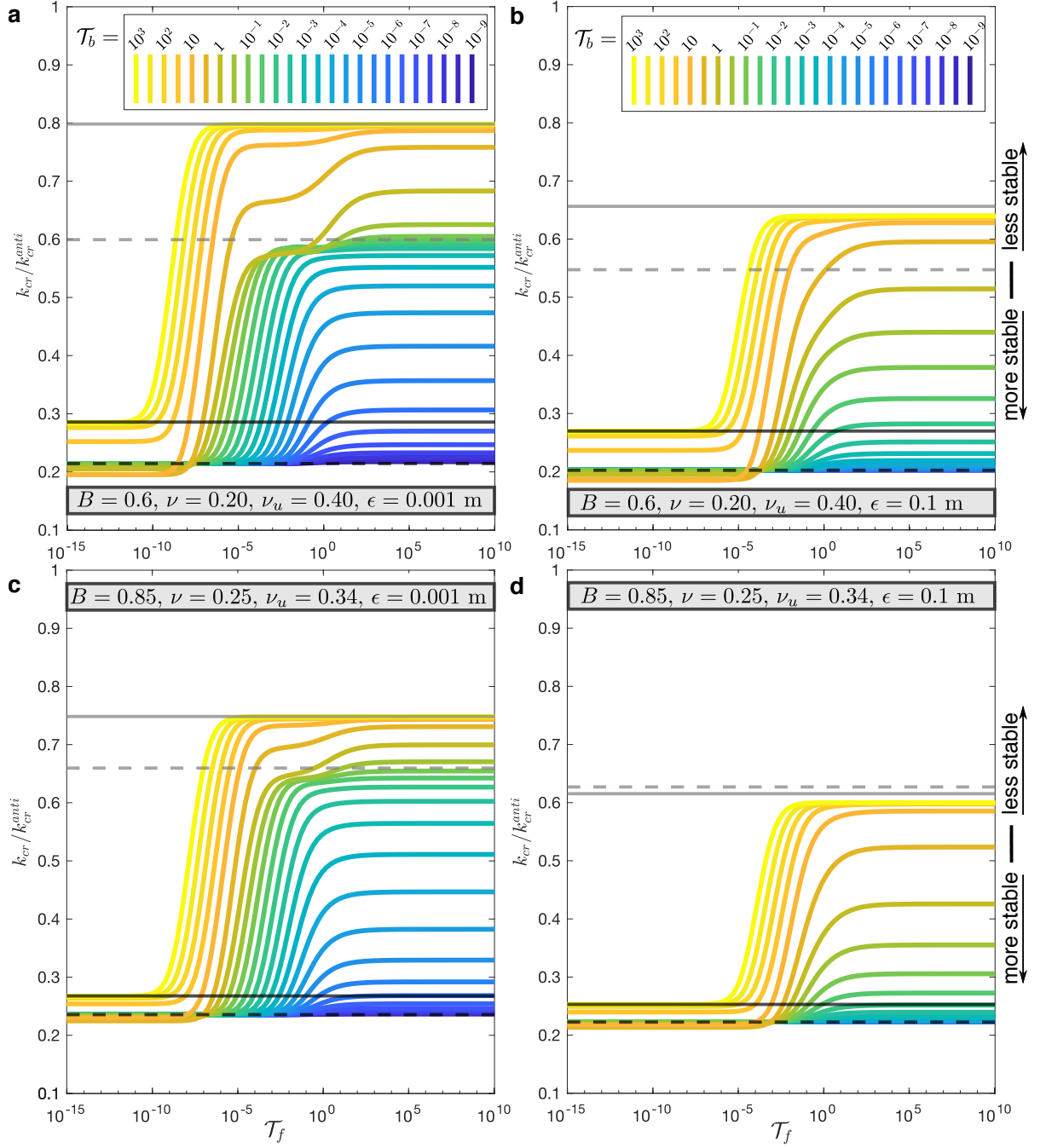


Figure 2. Changes in critical wavenumber k_{cr} , non-dimensionalized by k_{cr}^{anti} , when varying \mathcal{T}_f and keeping \mathcal{T}_b fixed at various values, for in-plane shear. The limit of the undrained bulk and $\kappa_c = 0$ (equation 53) is shown by black dashed line. The limit of the drained bulk and $\kappa_c = 0$ (equation 55) is shown by the black solid line. The dashed and solid grey lines indicate the results for the undrained and drained bulk, respectively, with the leading-order ϵ correction (equations 59 and 63). **a** Generic granite and thinner shear zone. **b** Generic granite and thicker shear zone. **c** Generic sandstone and thinner shear zone. **d** Generic sandstone and thicker shear zone. We generally observe that the numerical solution coincides with the relevant analytical estimates obtained, although, the estimate for the undrained bulk with the leading order ϵ correction only works well for the thinner shear zones.

623 Figure 2 illustrates how varying the non-dimensional flux time scale \mathcal{T}_f while fix-
 624 ing the non-dimensional bulk-diffusion time scale \mathcal{T}_b alters the critical wavenumber. Gen-
 625 erally, a low flux time scale, for example due to low permeability of the shear zone, trans-
 626 lates into more stabilized slip since dilatancy of the shear zone can increase the effective
 627 normal stress and increase the frictional resistance. However, this effect is not only con-
 628 trolled by the time scale of shear-zone flux, because a more diffusive bulk will limit the
 629 range at which dilatancy can stabilize sliding. However, in the extreme limit that the
 630 bulk diffusion is very fast, but flux is very small, dilatancy can still stabilize. See, for ex-
 631 ample, bright yellow line in Figure 2 or dark blue line in Figure 3. However, this limit
 632 is less stable than when both \mathcal{T}_f and \mathcal{T}_b are small, since the bulk response is drained and
 633 thus has effectively a lower Poisson’s ratio.

634 We clearly observe that the analytical estimates of section 4.2 derived for the limit
 635 of $\kappa_c = 0$ for drained and undrained bulk response generally hold in all cases when solv-
 636 ing the complete characteristic equation (Figures 2 and 3, black solid and dashed lines).
 637 However, in the case of a thicker shear zone (panels b and d), the critical wavenumber
 638 is even more reduced as a consequence of fault-normal displacements. Further, we see
 639 that the limit of drained bulk response and high flux (grey solid line) also has significance,
 640 although the first-order correction shows some mismatch in the cases with the thicker
 641 shear layer (panels b and d in Figures 2 and 3), indicating that higher-order terms are
 642 becoming important, as would be expected for a wider shear layer. We see that the cu-
 643 rious limit of high-flux but undrained bulk response (grey dashed line) is not an actual
 644 limiting case, but rather describes an intermediate stability characteristic in a certain
 645 parameter range for the thinner shear layer (panels a and c). This is not surprising, since
 646 the two time scales, \mathcal{T}_f and \mathcal{T}_b , are not perfectly independent, in the sense that the flux
 647 time scale also depends on the hydraulic diffusivity of the bulk. Thus a limit where the
 648 bulk can be considered undrained but the flux time scale is fast can only approximately
 649 hold over a certain range of time scales.

650 For the thicker shear layer (Figures 2 and 3, panels b and d), we find substantial
 651 stabilization in comparison with the thinner shear layer even in the limit of high flux and
 652 high bulk diffusivity (grey solid lines), which occurs due to the fault-normal displacements
 653 from dilatancy and the associated increase in normal stress on the shearing layer. Since
 654 this effect occurs even in the drained limit, it would also be predicted if the bulk were
 655 modeled as simple elastic material.

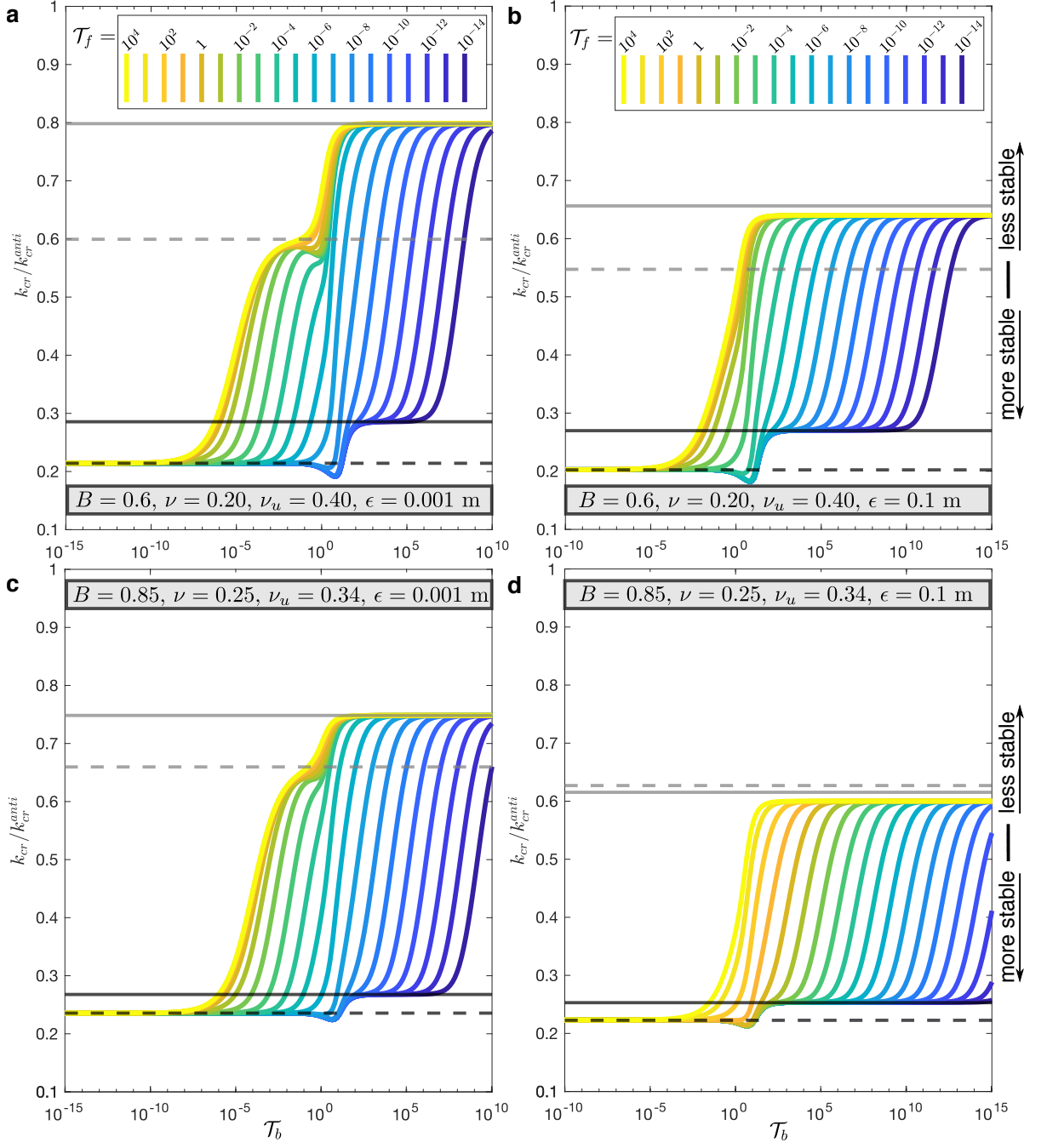


Figure 3. Changes in critical wavenumber k_{cr} , non-dimensionalized by k_{cr}^{anti} , when varying \mathcal{T}_b but keeping \mathcal{T}_f fixed, for in-plane shear. Definitions of lines and panels are the same as in Figure

2.

656 **6 Anti-plane sliding**

657 Here we explore the stability of the steady state for anti-plane sliding. Since equa-
658 tion 19 has no dependence on Poisson's ratio and no transient poroelastic response, we
659 observe much less variability in stability in the explored limiting cases than for the in-
660 plane sliding.

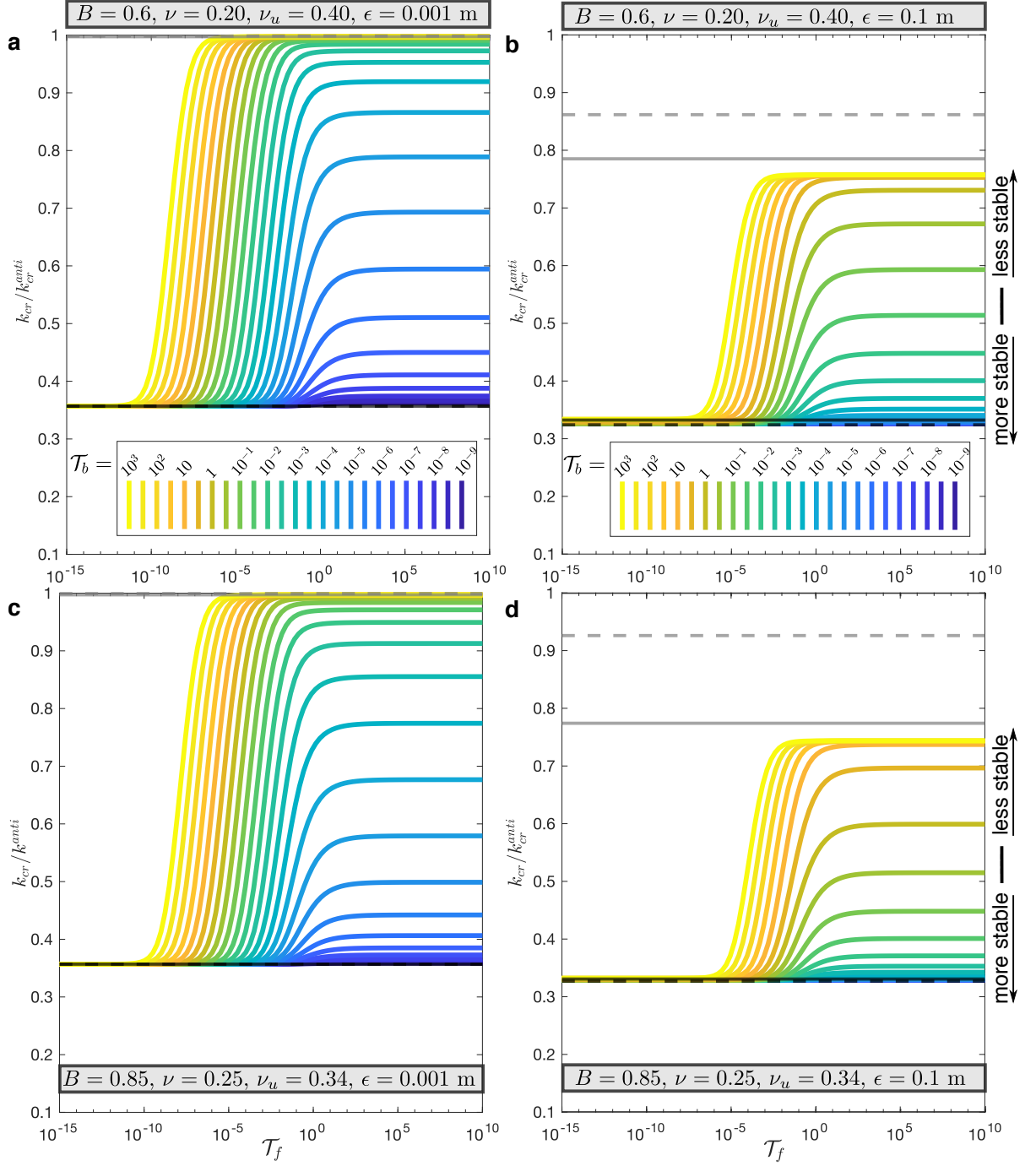


Figure 4. Changes in critical wavenumber k_{cr} , non-dimensionalized by k_{cr}^{anti} , when varying \mathcal{T}_f but keeping \mathcal{T}_b fixed, for anti-plane sliding. The black dashed line indicates an estimate of the critical wavenumber for the limit of the undrained bulk and $\kappa_c = 0$. Black solid line represents the critical wavenumber for drained bulk and $\kappa_c = 0$ limit (equation 57). Grey dashed line represents results for the undrained bulk with leading order ϵ correction (see equation 59 and following text). Solid grey line is the drained bulk with leading order ϵ correction (see equation 63 and following text). **a** generic granite and small shear zone. **b** generic granite and thick shear zone. **c** generic sandstone and thin shear zone. **d** generic sandstone and thick shear zone.

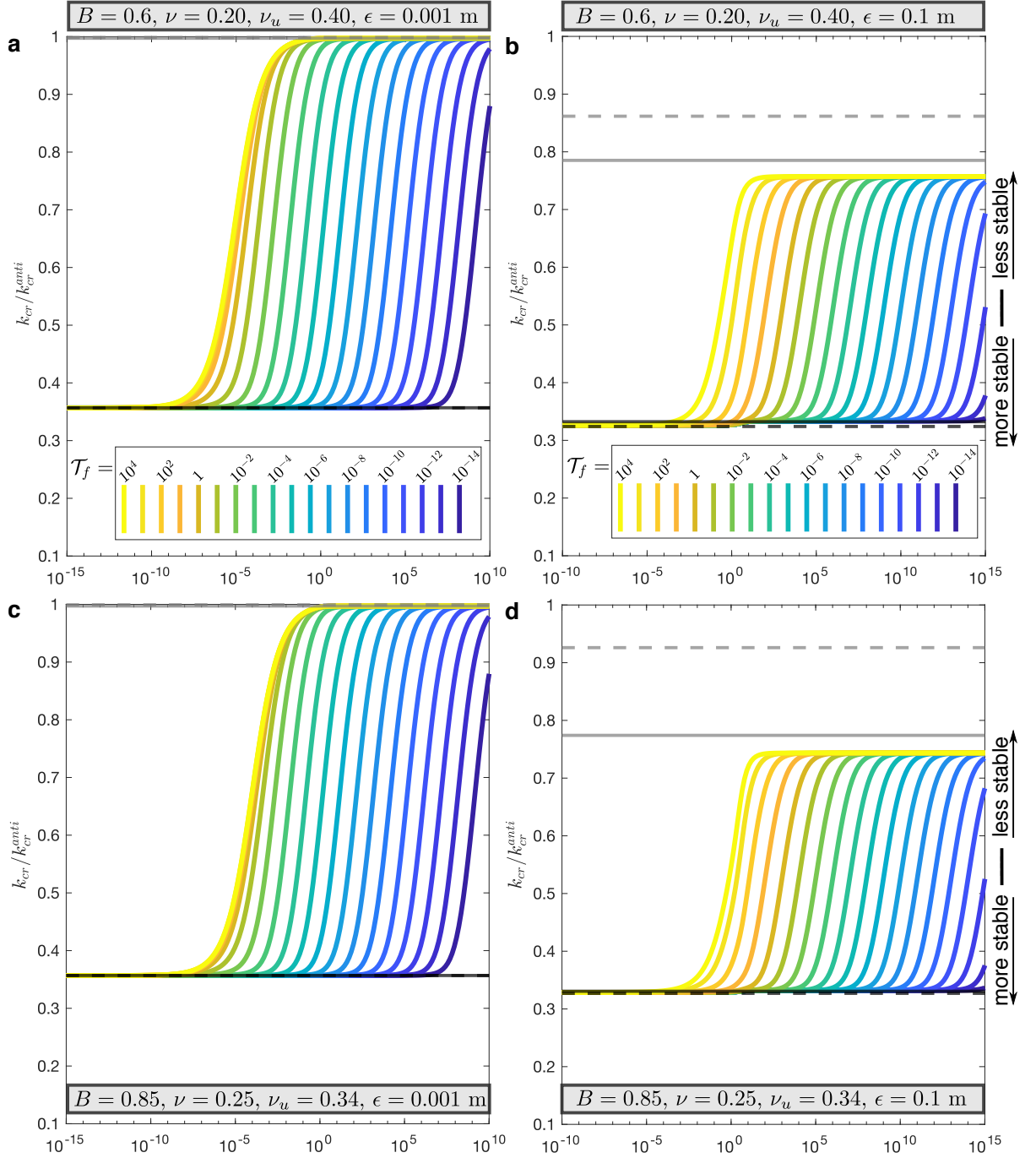


Figure 5. Changes in critical wavenumber k_{cr} , non-dimensionalized by k_{cr}^{anti} , when varying τ_b but keeping τ_f fixed, for anti-plane sliding. Definitions of lines and panels are the same as in Figure 4.

661 Figures 4 and 5 illustrate that, as expected, the anti-plane case is much simpler than
 662 the in-plane one. This is because the only difference in the drained and undrained bulk
 663 response in the anti-plane case arises from the differences in effective normal stress (equa-
 664 tions 20 and 21), but not through the sliding-induced shear stress changes (equation 19).
 665 This demonstrates that poroelasticity can play an important role in not only the nor-
 666 mal stress changes but also shear stress changes during rupture propagation or event nu-
 667 cleation. Nevertheless, all the same limits exist as for the in-plane case, except for the
 668 undrained bulk with high flux (grey dashed line).

669 **7 Discussion**

670 **7.1 Comparison with Segall and Rice (1995)**

671 This study is greatly influenced by the seminal work of Segall and Rice (1995), which
 672 showed that inelastic dilatancy can significantly stabilize sliding of a frictional interface.
 673 This theory has received particular notice since it offers a physical explanation for gener-
 674 ating slow slip events on faults (Segall et al., 2010). It is, therefore, worth summariz-
 675 ing and highlighting some of the differences between the analysis presented here and the
 676 original analysis of Segall and Rice (1995).

677 The most fundamental difference between the stability analysis in Segall and Rice
 678 (1995) and in our study is the treatment of the bulk. We present the stability analysis
 679 in a fully coupled poroelastic medium, whereas Segall and Rice (1995) used a single-degree-
 680 of-freedom spring-slider representation of the bulk. Thus, instead of solving for a crit-
 681 ical wavenumber (or wavelength) of a perturbation, they solved for the critical spring
 682 stiffness. Using elementary fracture mechanics for crack stiffness, one can interpret the
 683 spring-slider analysis in terms of the critical wavenumber (e.g., Dieterich, 1992). Indeed,
 684 our equation (57), for example, provides results completely consistent with the spring-
 685 slider analysis up to a scaling factor of order 1 and ignoring the $O(\epsilon)$ correction. How-
 686 ever, other aspects of the stability determined in this study cannot be captured with the
 687 spring-slider analysis, for example, the transient stability regimes where neither drained
 688 nor undrained response dominates (Figures 2, 3, 4, and 5). Such regimes depend on the
 689 wavenumber (equation 49), which changes one of the relevant diffusion times, and thus
 690 cannot be captured by rescaling of the critical stiffness (e.g., equations 16 and 17). In

691 Segall and Rice (1995), the transient stability regimes, controlled by a relevant diffusion
 692 time, do not depend on a length scale.

693 The second key difference is the presence of two time scales at which pressure equi-
 694 libration occurs. These are the time scale of pressure equilibration through shear layer
 695 flux \mathcal{T}_f , and the time scale related to the diffusion through the bulk \mathcal{T}_b . Segall and Rice
 696 (1995) and the alternative diffusion model in Segall et al. (2010) only have one diffusion
 697 time scale. The analysis with two diffusion time scales provides additional insights into
 698 the problem. For example, there is a parameter range where the bulk diffusion can be
 699 extremely fast and the bulk response can be considered drained. However, the shear-layer
 700 flux time scale is sufficiently slow such that dilatancy can act to stabilize sliding by re-
 701 ducing pore pressure and increasing effective normal stress. That limit may be of im-
 702 portant geological relevance. It has been frequently reported that the fault core, where
 703 shear localization occurs, has very low permeability (Caine et al., 1996; Wibberley & Shi-
 704 mamoto, 2003; Behnsen & Faulkner, 2011), while the adjacent damage zone is highly per-
 705 meable (F. Chester & Logan, 1986; Mitchell & Faulkner, 2012).

706 The final key difference, which is also discussed in some detail in the following sub-
 707 section, is that our study accounts for the fault-normal displacements that arise from di-
 708 latancy and pressure changes in the shear zone. This effect was not considered by Segall
 709 and Rice (1995), and it has not been studied previously in the fault mechanics literature
 710 to the best of our knowledge. As has been shown here, this effect gives rise to a differ-
 711 ent mechanism through which dilatancy can stabilize sliding.

712 **7.2 Fault-normal displacements**

713 Theoretical studies and field-based observations usually support the idea that seis-
 714 mic slip in fault gouge occurs in an extremely localized shear layer of 1 – 100 μm . The
 715 stability analysis and numerical simulations of Rice et al. (2014) and Platt et al. (2014)
 716 used a thermo-poro-mechanical model and suggested that the width of a shear zone arises
 717 as a competition between destabilizing thermal pressurization process and a stabilizing
 718 process that may be dilatancy or rate-strengthening friction. In the absence of a stabi-
 719 lizing process, the shear zone thickness becomes infinitesimal. Their findings are gener-
 720 ally supported in field observations. For example, J. S. Chester et al. (2005) examined
 721 the shear zone of the Punchbowl fault in California which has been exhumed from 2–

722 4 km depths and found the principal shear layer of 100-300 microns. De Paola et al. (2008)
723 examined cataclastic fault cores in the Northern Apennines and observed extreme shear
724 strain localization of some tens of microns. However, studies also suggest that the shear
725 layer can be wider. Boullier et al. (2009) examined two borehole cores, which intersected
726 the Chelungpu fault at about 1 km depth after the Chi-Chi earthquake in 1999. Their
727 analysis suggested thin shear localization zone from one core of 2 mm and the other 20
728 mm. While these widths are small compared to virtually all other characteristic dimen-
729 sions of that earthquake, it does suggest that even localization at seismic ruptures can
730 vary substantially.

731 In this study, we have focused on the stability around steady-state quasi-static (slow)
732 sliding. It is less clear how localized the shear zones are at creep rates in the range of
733 centimeters to millimeters per year. Laboratory experiments suggest that the width of
734 such localization depends on the normal stress, where a more delocalized shear-zone is
735 formed at low normal stress (Torabi et al., 2007). These observations beg the question
736 of how localized are the shear zones in regions of slow slip and tectonic tremor in sub-
737 duction zones. The same question applies to the roots of some strike-slip faults where
738 it has been suggested that pore pressure may be near lithostatic (e.g., Rubinstein et al.,
739 2007; Thomas et al., 2009). It has recently been argued that tectonic *mélanges*, some
740 hundreds of meters thick, may play an important role in aseismic slip processes along
741 the subduction zone interface (Fagereng et al., 2018; Raimbourg et al., 2019). It is not
742 clear if such large structures can be regarded as a single shear zone and would thus fall
743 under the scope of our analysis. However, geological observations of *mélanges* strongly
744 suggest that not all shear strain on faults occurs in extremely localized zones.

745 If the shear layers are sufficiently thick during quasi-static shear, as appears to be
746 possible from lab and field observations, then they can generate fault-normal displace-
747 ments that stabilize sliding. These displacements are largely caused by the same dila-
748 tancy process that reduces pore pressure in the shear zone. The additional stabilization
749 due to fault-normal displacements occurs because the shear layer must expand against
750 the stiff host rock and that increases the normal stress on the layer and hence its resis-
751 tance to sliding. Order-of-magnitude estimates of various parameters suggest that the
752 shear zone thickness produces significant stabilizing fault-normal displacements through
753 dilatancy if $\epsilon \gtrsim 0.1L/\gamma$. Taking $L \sim 10 \mu\text{m}$ and $\gamma \sim 10^{-4}$ indicates that the shear

754 layer of the width $\epsilon \sim 1$ cm can be considered an approximate threshold at which fault-
 755 normal displacements are large enough to produce a significant stabilizing effect.

756 We hypothesize that, during shear localization, the fault-normal motion may de-
 757 lay or perhaps prevent further localization, since a perturbation, which otherwise could
 758 induce an instability process with extreme localization, may be stabilized by the (larger)
 759 shear-zone width at that time. Note that the conclusions may be different for other as-
 760 sumptions of the relevant pore pressure values within the fault zone, such as taking the
 761 largest value of pore fluid pressure, which would promote localization. Other factors not
 762 considered in this study may affect shear localization, such as thermal pressurization of
 763 pore fluids considered in Rice et al. (2014) and Platt et al. (2014).

764 8 Conclusions

765 The stabilizing effect of dilatancy on slip along a frictional fault has garnered in-
 766 terest since the mechanism was proposed and formulated by Segall and Rice (1995) within
 767 the scope of the rate-and-state friction framework. While a number of studies have im-
 768 plemented dilatancy in simulations of slow and fast slip on faults with rate-and-state fric-
 769 tion, the implementation and formulation of dilatancy in a fully-coupled poroelastic solid
 770 has been missing. Here we present a closed system of equation describing a shearing gouge
 771 layer under in-plane and anti-plane loading with rate-and-state dependent friction and
 772 undergoing state-dependent dilatancy/compaction.

773 We have presented a linearized analysis of the stability of shearing in the layer around
 774 steady state. We have identified two mechanisms through which dilatancy can stabilize
 775 frictional sliding: first, by reducing pore pressure in the shearing layer and second, by
 776 expanding the layer and generating fault-normal displacements in the bulk. The former
 777 mechanism was identified by Segall and Rice (1995), where they show that it is most ef-
 778 fective for an undrained bulk with loss of stabilization as the bulk response approaches
 779 the drained limit. We add to this criterion by highlighting that such stabilization can
 780 occur even if the bulk is highly diffusive and responds in a drained manner, due to lower
 781 flux within the shear layer. The latter mechanism, due to fault-normal displacements,
 782 has not been identified previously, to the best of our knowledge. It primarily results from
 783 dilatancy-induced expansion of the shear zone. The expanding shear zone presses against
 784 the host rock and increases normal stress acting on the shear zone, thus increasing fric-

785 tional resistance. This effect does not require the presence of pore pressure changes and
 786 occurs even if the shear zone and bulk responses are drained.

787 The results of this study highlight the importance of considering the realistic hydro-
 788 mechanical structure of faults around the thin shear layers, including the actual width
 789 of the shearing layer as well as the potential difference between the hydraulic diffusiv-
 790 ity of the shear layer (which is thin but finite) and the surrounding host rock. The iden-
 791 tified stability properties near steady-state sliding will inform future numerical explo-
 792 rations of the full non-linear problem of a shear fault sliding with dilatancy/compaction
 793 in a poroelastic solid.

794 **Acknowledgments**

795 This study was supported by the Geophysics Option Postdoctoral Fellowship from the
 796 Division of Geological and Planetary Sciences at Caltech to E.R.H. and by the NSF-IUCRC
 797 Center for Geomechanics and Mitigation of Geohazards (projects GMG-4.1, GMG-4.2)
 798 to N.L. This is a theoretical paper and contains no data. Code for determining the crit-
 799 ical stability and solving equation 41, which also contains explicit expression for equa-
 800 tion to long to write out in this paper, is found here
 801 <http://doi.org/10.5281/zenodo.4609838> (see Heimisson, 2021)

802 **Appendix A Parameter values**

803 Here we discuss the parameters that are kept constant when we numerically solve
 804 for the roots of the characteristic equations at critical stability, as shown in Figures 2,
 805 3, 4, and 5. These parameters and their values are summarized in Table A1.

806 The material parameters that are fixed are the shear modulus G of the bulk, var-
 807 ious compressibilities of the gouge, and the reference porosity of the gouge at steady state
 808 sliding ϕ_0 , which is assumed to be equivalent to the reference void volume per unit vol-
 809 ume. We use $G = 30$ GPa which is selected somewhat arbitrarily but which is a com-
 810 mon value used for crustal rocks and should be applicable to well-packed fault gouge.
 811 The other bulk poroelastic parameters are varied and explained in the main text. It is
 812 worth noting that, to explore different values of the non-dimensional parameter \mathcal{T}_f in
 813 Figures 2, 3, 4, and 5 we only change κ_c but, to explore different values of \mathcal{T}_b , we change

814 both the hydraulic diffusivity of the bulk and κ_c so that \mathcal{T}_f is fixed (since it depends on
 815 both c and κ_c), in accordance with equations 52 and 51.

816 In selecting the various gouge material properties, we broadly follow Segall and Rice
 817 (1995), Rice et al. (2014), and Platt et al. (2014) where appropriate. We take $\beta_f^p = 0.44 \cdot$
 818 10^{-9} Pa^{-1} (Fine & Millero, 1973). We use $\beta_n^p = 6.0 \cdot 10^{-9} \text{ Pa}^{-1}$ which Rice et al. (2014)
 819 and Platt et al. (2014) inferred to be appropriate for damaged rocks based on the data
 820 by Wibberley and Shimamoto (2003) and using the analysis of Rice (2006). The com-
 821 pressibility of the gouge grains, β_g^p , has not, to the best of our knowledge, been featured
 822 in previous literature. We expect this compressibility to be low compared to the fluid
 823 or pore compressibilities. We simply assume that it is the inverse of a typical rock bulk
 824 modulus of 50 GPa, that is, $\beta_g^p = 0.02 \cdot 10^{-9} \text{ Pa}^{-1}$. The uniaxial compressibilities β_f^σ ,
 825 β_n^σ , and β_g^σ have not received much attention in the previous literature. Here we assume
 826 that we can obtain the uniaxial compressibility by multiplying the isotropic compressibil-
 827 ity by a factor of 5/9. As discussed in the main text, this is only strictly true for a lin-
 828 ear elastic material. However, this likely offers a reasonable correspondence between isotropic
 829 and uniaxial compressibility more generally. Nevertheless, we suggest that more stud-
 830 ies are needed to determine if uniaxial compressibilities can be vastly different from the
 831 isotropic compressibilities. We select the reference porosity at steady-state sliding, also
 832 interpreted as the void volume per unit volume, as $\phi = 0.068$. This is a commonly used
 833 value based on Wibberley and Shimamoto (2003). Finally, we follow Segall and Rice (1995)
 834 in their modeling of the Marone et al. (1990) experiments and select the dilatancy co-
 835 efficient as $\gamma = 1.7 \cdot 10^{-4}$.

836 For the friction and fault loading parameters, we select fairly standard values (Ta-
 837 ble A1) frequently used in the literature. It is worth mentioning that, for simplicity, we
 838 have taken the Linker and Dieterich (1992) constant $\alpha_{LD} = 0$, which implies no explicit
 839 dependence of the state variable on normal stress changes. This essentially means that
 840 we consider the effective normal stress changes to be gradual enough that the shear stress
 841 stays proportional to the effective normal stress, a reasonable assumption given the slow
 842 slip considered. In Table A1, we provide both initial shear and normal stress for conve-
 843 nience, but the two are not independent due to the condition that the fault is initially
 844 at steady state and are related through $\tau_0 = f_0 \sigma_0$.

Table A1. Parameters that are kept constant in the study

Symbol	Description	Value
<i>Bulk and gouge material properties</i>		
G	Shear modulus	30 GPa
$\beta_f^p, \beta_f^\sigma$	Isotropic and uniaxial fluid compressibility	$0.44 \cdot 10^{-9} \text{ Pa}^{-1}$, $0.24 \cdot 10^{-9} \text{ Pa}^{-1}$,
$\beta_n^p, \beta_n^\sigma$	Isotropic and uniaxial pore volume compressibility	$6.0 \cdot 10^{-9} \text{ Pa}^{-1}$, $3.3 \cdot 10^{-9} \text{ Pa}^{-1}$,
$\beta_g^p, \beta_g^\sigma$	Isotropic and uniaxial solid gouge compressibility	$0.020 \cdot 10^{-9} \text{ Pa}^{-1}$, $0.011 \cdot 10^{-9} \text{ Pa}^{-1}$,
ϕ_0	Reference porosity	0.068
<i>Friction and loading parameters</i>		
L	Characteristic state evolution distance	100 μm
a	Direct rate dependence of friction	0.01
b	State dependence of friction	0.02
α_{LD}	Linker and Dieterich (1992) constant	0.0
V_0	Steady-state and reference sliding velocity	10^{-9} m/s
f_0	Steady-state coefficient of friction at V_0	0.6
τ_0	Initial shear stress	20.0 MPa
σ_0	Initial effective normal stress	33.3 MPa

845 Throughout the main text, we have mostly used G , B , ν , ν_u , c to fully describe the
846 poroelastic bulk properties. However, in a few cases, we have used different set of pa-
847 rameter for compactness, that is, M , α , and κ . Here we list a few relationships that would
848 allow the reader to convert between these parameter sets:

$$B = \frac{3M\alpha(1-2\nu)}{2G(1+\nu) + 3M\alpha^2(1-2\nu)}$$

$$\nu_u = \frac{2G\nu + M\alpha^2(1-2\nu)}{2G + 2M\alpha^2(1-2\nu)}$$

$$B = \frac{3(\nu_u - \nu)}{\alpha(1-2\nu)(1+\nu_u)}$$

$$c = M\kappa.$$

849 **References**

- 850 Behnsen, J., & Faulkner, D. (2011). Water and argon permeability of phyllosilicate
851 powders under medium to high pressure. *Earth Planet. Sc. Lett.*, *116*(B12).
- 852 Bhattacharya, P., & Viesca, R. C. (2019). Fluid-induced aseismic fault slip out-
853 paces pore-fluid migration. *Science*, *364*(6439), 464–468. doi: 10.1126/science
854 .aaw7354
- 855 Boullier, A.-M., Yeh, E.-C., Boutareaud, S., Song, S.-R., & Tsai, C.-H. (2009). Mi-
856 croscale anatomy of the 1999 chi-chi earthquake fault zone. *Geochemistry,*
857 *Geophysics, Geosystems*, *10*(3). doi: 10.1029/2008GC002252
- 858 Bürgmann, R. (2018). The geophysics, geology and mechanics of slow fault slip.
859 *Earth Planet. Sc. Lett.*, *495*, 112–134.
- 860 Caine, J. S., Evans, J. P., & Forster, C. B. (1996). Fault zone architecture and per-
861 meability structure. *Geology*, *24*(11), 1025–1028.
- 862 Chester, F., & Logan, J. M. (1986). Implications for mechanical properties of brit-
863 tle faults from observations of the punchbowl fault zone, california. *Pure Appl.*
864 *Geophys.*, *124*(1-2), 79–106.
- 865 Chester, F. M., Chester, J. S., Kirschner, D. L., Schulz, S. E., & Evans, J. P. (2004).
866 Structure of large-displacement, strike-slip fault zones in the brittle continental
867 crust. *Rheology and deformation in the lithosphere at continental margins*, *1*,
868 223–260.
- 869 Chester, F. M., Evans, J. P., & Biegel, R. L. (1993). Internal structure and weaken-
870 ing mechanisms of the san andreas fault. *J. Geophys. Res.*, *98*(B1), 771–786.
- 871 Chester, J. S., Chester, F. M., & Kronenberg, A. K. (2005). Fracture surface energy
872 of the punchbowl fault, san andreas system. *Nature*, *437*(7055), 133–136.
- 873 Ciardo, F., & Lecampion, B. (2019). Effect of dilatancy on the transition from
874 aseismic to seismic slip due to fluid injection in a fault. *Journal of Geophys-*
875 *ical Research: Solid Earth*, *124*(4), 3724–3743. doi: [https://doi.org/10.1029/
876 2018JB016636](https://doi.org/10.1029/2018JB016636)
- 877 Cocco, M., & Rice, J. R. (2002). Pore pressure and poroelasticity effects in coulomb
878 stress analysis of earthquake interactions. *Journal of Geophysical Research:*
879 *Solid Earth*, *107*(B2), ESE 2-1-ESE 2-17. doi: [https://doi.org/10.1029/
880 2000JB000138](https://doi.org/10.1029/2000JB000138)
- 881 Dal Zilio, L., Lapusta, N., & Avouac, J.-P. (2020). Unraveling scaling prop-

- 882 erties of slow-slip events. *Geophysical Research Letters*, 47(10). doi:
883 10.1029/2020GL087477
- 884 De Paola, N., Collettini, C., Faulkner, D. R., & Trippetta, F. (2008). Fault zone
885 architecture and deformation processes within evaporitic rocks in the upper
886 crust. *Tectonics*, 27(4). doi: 10.1029/2007TC002230
- 887 Detournay, E., & Cheng, A. H.-D. (1995). Fundamentals of poroelasticity. In *Analy-*
888 *sis and design methods* (pp. 113–171). Elsevier.
- 889 Dieterich, J. H. (1979). Modeling of rock friction: 1. experimental results and consti-
890 tutive equations. *Journal of Geophysical Research: Solid Earth*, 84(B5), 2161-
891 2168. doi: 10.1029/JB084iB05p02161
- 892 Dor, O., Rockwell, T. K., & Ben-Zion, Y. (2006, Mar 01). Geological observations
893 of damage asymmetry in the structure of the San Jacinto, San Andreas and
894 Punchbowl faults in Southern California: A possible indicator for preferred
895 rupture propagation direction. *Pure Appl. Geophys.*, 163(2), 301–349. doi:
896 10.1007/s00024-005-0023-9
- 897 Dunham, E. M., & Rice, J. R. (2008). Earthquake slip between dissimilar poroelas-
898 tic materials. *J. Geophys. Res. Solid Earth*, 113(B9). (B09304) doi: 10.1029/
899 2007JB005405
- 900 Ellsworth, W. L. (2013). Injection-induced earthquakes. *Science*, 341(6142),
901 1225942.
- 902 Fagereng, Á., Diener, J. F., Ellis, S., & Remitti, F. (2018). *Fluid-related deformation*
903 *processes at the up-and down-dip limits of the subduction thrust seismogenic*
904 *zone: What do the rocks tell us* (Vol. 534). Geol. Soc. Am. Spec. Pap.
- 905 Ferdowsi, B., & Rubin, A. M. (2020). A granular physics-based view of fault fric-
906 tion experiments. *Journal of Geophysical Research: Solid Earth*, 125(6),
907 e2019JB019016. doi: <https://doi.org/10.1029/2019JB019016>
- 908 Fine, R. A., & Millero, F. J. (1973). Compressibility of water as a function
909 of temperature and pressure. *The Journal of Chemical Physics*, 59(10),
910 5529-5536. Retrieved from <https://doi.org/10.1063/1.1679903> doi:
911 10.1063/1.1679903
- 912 Heimisson, E. R. (2021, March). *eliasrh/Poroelastic_linear_stability: Release for pub-*
913 *lication of Heimisson, Rudnicki, and Lapusta 2021*. Zenodo. Retrieved from
914 <https://doi.org/10.5281/zenodo.4609838> doi: 10.5281/zenodo.4609838

- 915 Heimissson, E. R., Dunham, E. M., & Almquist, M. (2019). Poroelastic effects
 916 destabilize mildly rate-strengthening friction to generate stable slow slip
 917 pulses. *Journal of the Mechanics and Physics of Solids*, *130*, 262 – 279. doi:
 918 10.1016/j.jmps.2019.06.007
- 919 Heimissson, E. R., & Segall, P. (2018). Constitutive law for earthquake production
 920 based on rate-and-state friction: Dieterich 1994 revisited. *Journal of Geophysi-
 921 cal Research: Solid Earth*, *123*(5), 4141–4156. doi: 10.1029/2018JB015656
- 922 Hulikal, S., Lapusta, N., & Bhattacharya, K. (2018). Static and sliding contact of
 923 rough surfaces: Effect of asperity-scale properties and long-range elastic in-
 924 teractions. *Journal of the Mechanics and Physics of Solids*, *116*, 217 - 238.
 925 Retrieved from [http://www.sciencedirect.com/science/article/pii/
 926 S0022509618300619](http://www.sciencedirect.com/science/article/pii/S0022509618300619) doi: <https://doi.org/10.1016/j.jmps.2018.03.022>
- 927 Jha, B., & Juanes, R. (2014). Coupled multiphase flow and poromechanics:
 928 A computational model of pore pressure effects on fault slip and earth-
 929 quake triggering. *Water Resources Research*, *50*(5), 3776-3808. doi:
 930 10.1002/2013WR015175
- 931 Jónsson, S., Segall, P., Pedersen, R., & Björnsson, G. (2003). Post-earthquake
 932 ground movements correlated to pore-pressure transients. *Nature*, *424*(6945),
 933 179–183. doi: 10.1038/nature01776
- 934 Linker, M. F., & Dieterich, J. H. (1992). Effects of variable normal stress on rock
 935 friction: Observations and constitutive equations. *J. Geophys. Res. Solid
 936 Earth*, *97*(B4), 4923–4940. doi: 10.1029/92JB00017
- 937 Liu, Y. (2013). Numerical simulations on megathrust rupture stabilized under strong
 938 dilatancy strengthening in slow slip region. *Geophysical Research Letters*,
 939 *40*(7), 1311-1316. doi: 10.1002/grl.50298
- 940 Lockner, D. A., & Byerlee, J. D. (1994). Dilatancy in hydraulically isolated faults
 941 and the suppression of instability. *Geophysical Research Letters*, *21*(22), 2353-
 942 2356. doi: 10.1029/94GL02366
- 943 Marone, C. (1998). Laboratory-derived friction laws and their application to seismic
 944 faulting. *Annu. Rev. Earth Pl. Sc.*, *26*(1), 643–696.
- 945 Marone, C., Raleigh, C. B., & Scholz, C. H. (1990). Frictional behavior and con-
 946 stitutive modeling of simulated fault gouge. *Journal of Geophysical Research:
 947 Solid Earth*, *95*(B5), 7007-7025. doi: 10.1029/JB095iB05p07007

- 948 McNamee, J., & Gibson, R. E. (1960). Plane strain and axially symmetric problems
 949 of the consolidation of a semi-infinite clay stratum. *Q. J. Mech. Appl. Math.*,
 950 *13*(2), 210–227.
- 951 Mitchell, T., & Faulkner, D. (2012). Towards quantifying the matrix permeability of
 952 fault damage zones in low porosity rocks. *Earth Planet. Sc. Lett.*, *339*, 24–31.
- 953 Platt, J. D., Rudnicki, J. W., & Rice, J. R. (2014). Stability and localization of
 954 rapid shear in fluid-saturated fault gouge: 2. localized zone width and strength
 955 evolution. *Journal of Geophysical Research: Solid Earth*, *119*(5), 4334–4359.
 956 doi: 10.1002/2013JB010711
- 957 Proctor, B., Lockner, D. A., Kilgore, B. D., Mitchell, T. M., & Beeler, N. M. (2020).
 958 Direct evidence for fluid pressure, dilatancy, and compaction affecting slip in
 959 isolated faults. *Geophysical Research Letters*, *47*(16), e2019GL086767. doi:
 960 10.1029/2019GL086767
- 961 Raimbourg, H., Famin, V., Palazzin, G., Yamaguchi, A., Augier, R., Kitamura,
 962 Y., & Sakaguchi, A. (2019). Distributed deformation along the subduction
 963 plate interface: The role of tectonic mélanges. *Lithos*, *334–335*, 69–87. doi:
 964 <https://doi.org/10.1016/j.lithos.2019.01.033>
- 965 Rice, J. R. (2006). Heating and weakening of faults during earthquake slip. *Journal*
 966 *of Geophysical Research: Solid Earth*, *111*(B5). doi: 10.1029/2005JB004006
- 967 Rice, J. R., & Cleary, M. P. (1976). Some basic stress diffusion solutions for fluid-
 968 saturated elastic porous media with compressible constituents. *Rev. Geophys.*,
 969 *14*(2), 227–241. doi: 10.1029/RG014i002p00227
- 970 Rice, J. R., Lapusta, N., & Ranjith, K. (2001). Rate and state dependent friction
 971 and the stability of sliding between elastically deformable solids. *J. Mech.*
 972 *Phys. Solids*, *49*(9), 1865–1898.
- 973 Rice, J. R., Rudnicki, J. W., & Platt, J. D. (2014). Stability and localization
 974 of rapid shear in fluid-saturated fault gouge: 1. linearized stability analy-
 975 sis. *Journal of Geophysical Research: Solid Earth*, *119*(5), 4311–4333. doi:
 976 10.1002/2013JB010710
- 977 Rice, J. R., & Ruina, A. (1983). Stability of steady frictional slipping. *J. Appl.*
 978 *Mech.*, *50*(2), 343–349.
- 979 Rice, J. R., & Simons, D. A. (1976). The stabilization of spreading shear faults
 980 by coupled deformation-diffusion effects in fluid-infiltrated porous materials. *J.*

- 981 *Geophys. Res.*, 81(29), 5322-5334. doi: 10.1029/JB081i029p05322
- 982 Rubinstein, J. L., Vidale, J. E., Gomberg, J., Bodin, P., Creager, K. C., & Malone,
983 S. D. (2007). Non-volcanic tremor driven by large transient shear stresses.
984 *Nature*, 448(7153), 579.
- 985 Rudnicki, J. W., & Chen, C.-H. (1988). Stabilization of rapid frictional slip on a
986 weakening fault by dilatant hardening. *Journal of Geophysical Research: Solid*
987 *Earth*, 93(B5), 4745–4757. doi: 10.1029/JB093iB05p04745
- 988 Rudnicki, J. W., & Koutsibelas, D. A. (1991). Steady propagation of plane strain
989 shear cracks on an impermeable plane in an elastic diffusive solid. *Int. J.*
990 *Solids Struct.*, 27(2), 205–225.
- 991 Rudnicki, J. W., & Rice, J. R. (2006). Effective normal stress alteration due to
992 pore pressure changes induced by dynamic slip propagation on a plane be-
993 tween dissimilar materials. *J. Geophys. Res. Solid Earth*, 111(B10). doi:
994 10.1029/2006JB004396
- 995 Ruina, A. (1983). Slip instability and state variable friction laws. *Jour-*
996 *nal of Geophysical Research: Solid Earth*, 88(B12), 10359-10370. doi:
997 10.1029/JB088iB12p10359
- 998 Segall, P., & Lu, S. (2015). Injection-induced seismicity: Poroelastic and earthquake
999 nucleation effects. *J. Geophys. Res. Solid Earth*, 120(7), 5082–5103.
- 1000 Segall, P., & Rice, J. R. (1995). Dilatancy, compaction, and slip instability of a
1001 fluid-infiltrated fault. *Journal of Geophysical Research: Solid Earth*, 100(B11),
1002 22155–22171. doi: 10.1029/95JB02403
- 1003 Segall, P., Rubin, A. M., Bradley, A. M., & Rice, J. R. (2010). Dilatant strength-
1004 ening as a mechanism for slow slip events. *J. Geophys. Res. Solid Earth*,
1005 115(B12).
- 1006 Song, Y., & Rudnicki, J. W. (2017). Plane-strain shear dislocation on a leaky plane
1007 in a poroelastic solid. *J. Appl. Mech.*, 84(2), 021008.
- 1008 Thomas, A. M., Nadeau, R. M., & Bürgmann, R. (2009). Tremor-tide correlations
1009 and near-lithostatic pore pressure on the deep san andreas fault. *Nature*,
1010 462(7276), 1048–1051. doi: 10.1038/nature08654
- 1011 Torabi, A., Braathen, A., Cuisiat, F., & Fossen, H. (2007). Shear zones in porous
1012 sand: Insights from ring-shear experiments and naturally deformed sandstones.
1013 *Tectonophysics*, 437(1), 37 - 50. doi: 10.1016/j.tecto.2007.02.018

- 1014 Torberntsson, K., Stiernström, V., Mattsson, K., & Dunham, E. M. (2018, Jul 19).
1015 A finite difference method for earthquake sequences in poroelastic solids. *Com-*
1016 *putat. Geosci.*, *22*(5), 1351–1370. doi: 10.1007/s10596-018-9757-1
- 1017 Verruijt, A. (1971). Displacement functions in the theory of consolidation or in ther-
1018 moelasticity. *Zeitschrift für angewandte Mathematik und Physik ZAMP*, *22*(5),
1019 891–898.
- 1020 Viesca, R. C., & Dublanquet, P. (2019). The slow slip of viscous faults. *Journal of*
1021 *Geophysical Research: Solid Earth*, *124*(5), 4959–4983. doi: [https://doi.org/10](https://doi.org/10.1029/2018JB016294)
1022 [.1029/2018JB016294](https://doi.org/10.1029/2018JB016294)
- 1023 Wibberley, C. A., & Shimamoto, T. (2003). Internal structure and permeability
1024 of major strike-slip fault zones: the Median Tectonic Line in Mie Prefecture,
1025 Southwest Japan. *J. Struct. Geol.*, *25*(1), 59–78.